Nanoscale features revealed by a multiscale characterization of discordant monazite highlight mobility mechanisms of Th and Pb

Marion J Turuani, Anne-Magali Seydoux-Guillaume, Antonin T Laurent, Steve Reddy, Simon Harley, Denis Fougerouse, David Saxey, Sophie Gouy, P. de Parseval, S. Reynaud, et al.

Nanoscale features revealed by a multiscale characterization of discordant monazite highlight mobility mechanisms of Th and Pb

M.J. Turuani[*1](0000-0002-8955-2674), A-M. Seydoux-Guillaume[1](0000-0002-9921-4695), A.T. Laurent[1](0000-0002-6202-2788),), S.M. Reddy[2,3](0000-0002-4726-5714), S.L. Harley[4](0000-0002-1903-939X), D. Fougerouse[2,3](0000-0003-3346-1121), D. Saxey[3](0000-0001-7433-946X), S. Gouy[5], P. De Parseval[5](0000-0003-4061-7526), S. Reynaud[6], W. Rickard[3](0000-0002-8118-730X)

[*]corresponding author. Present address: ISTerre, UGA, F-38058 Grenoble Cedex9, France; marion.turuani@univ-grenoble-alpes.fr

[1]UJM, CNRS, LGL-TPE, F-42023, Saint Etienne, France

[2]School of Earth and Planetary Sciences, Curtin University, Perth, Western Australia 6845, Australia

[3]Geoscience Atom Probe, John de Laeter Centre, Curtin University, Perth, Western Australia 6845, Australia

[4]School of Geosciences, University of Edinburgh, Edinburgh EH9 3FE, UK

[5]Géosciences Environnement Toulouse, GET/OMP (CNRS, UT3, IRD, CNES), Toulouse, France

[6]UJM, CNRS, Laboratoire Hubert Curien UMR 5516, F-42023 Saint-Etienne, France

Abstract

Understanding radionuclides mass transfer mechanisms in monazite ($LREEPO_4$) and the resulting features, from the micro- to the nanoscale, is critical to its use as a robust U–Th–Pb geochronometer. A detailed multi-scale characterization of discordant monazite grains from a granulite which records a polymetamorphic history, explores the mechanisms of Th and Pb mobility in crystals. Some monazite grains display Th-rich linear features (0.1-1 µm thick) forming a regular network throughout the grain. They are interpreted as resulting from fluid ingress along crystallographically-controlled pathways. Nanoscale features termed 'clusters' (Ø < 10 nm) are composed of radiogenic Pb (Pb*) ±Si ±Ca and are localised within monazite lattice defects. Their formation results from the competition, over millions of years, of both radiation damage production allowing element mobility (by diffusion) and accumulation in defects and α-healing inducing their trapping. Nanophases (Ø = 0.02-1 µm) containing Pb* are present in all grains and correspond to galena (PbS) or sesquioxide of Pb (Pb_2O_3). They are

associated with a chemically varied suite of amorphous silicate (±Al, Mg, Fe) phases or sulphur (e.g. FeS). They are interpreted as precipitates within monazite crystals. They formed during replacement mechanism of monazite through fluid interactions. Two generations of Pb*-bearing nanophases exist supported by previous geochronological data. The shielding effect of garnet and rutilated quartz (host minerals), limiting fluid access, induces plentiful Pb*-bearing nanophases precipitation (fluid saturation enhanced) and limits Pb*-loss at the grainscale. This multi-scale study provides new insights for interpretations of meaningless geochronological information thanks to nanoscale investigations.

Keywords: monazite – Napier complex (Antarctica) - Th and Pb mobility mechanisms – Pb-bearing nanophases – clusters –atom probe tomography and TEM

Introduction

The fundamental assumption for the use of minerals as geochronometers is that U, Th and especially their decay product Pb (Pb*) are immobile within the crystal lattice over time, so that an analysed domain represents a volume in which isotopic equilibria are conserved. However, examples of Pb mobility have been reported from mineral geochronometers in polymetamorphic terrains, leading to the formation of nanophases (Seydoux-Guillaume et al. 2003, 2019; Kusiak et al. 2015; Fougerouse et al. 2018) or nanoscale heterogeneous domains within the crystallographic lattice (Valley et al. 2014, 2015; Peterman et al. 2016; Verberne et al. 2020; Černok et al. 2021). The presence of such nanoscale features implies heterogeneity in the analytical volumes sampled in most microscale dating methods (e.g. laser ablation inductively coupled plasma mass spectrometry, LA-ICP-MS; Secondary Ion Mass Spectrometry, SIMS). This has the potential to impact on the calculated dates, and result in apparently disturbed isotopic datasets (Seydoux-Guillaume et al. 2003; Kusiak et al. 2013, 2015; Peterman et al. 2016).

Evidence of mineralogical processes that affect geochronometers and that induce element mobility may be recorded within the crystal. The benefits of examining geochronometers at the nanoscale using transmission electron microscopy (TEM) and atom probe tomography (APT) to address broader issues of element mobility has been demonstrated for zircon (Utsunomiya et al. 2004; Kusiak et al. 2015, 2019; Valley et al. 2015; Peterman et al. 2016, 2019; Piazolo et al. 2016; Whitehouse et al. 2017), monazite (Seydoux-Guillaume et al. 2003, 2019; Fougerouse et al. 2018, 2021a, b; Budzyń et al. 2021, 2022; Turuani et al. 2022), rutile (Verberne et al. 2020), xenotime (Joseph et al. 2021; Budzyń et al. 2023) and baddeleyite (White et al. 2017). Depending on the geological events that have affected the host rocks and geochronometers (e.g. thermal event, deformation), their characterization may afford a refined understanding of the processes involved in element mobility.

In monazite, diffusion-controlled element mobility is generally inefficient at the grain scale at most crustal temperatures, whereas it should be ubiquitous at the nanoscale. According to experimental data it would take ~6 Gyr to lose all the Pb from a 10 µm size grain at ~800°Ccompared to 0.04 Myr and 12 Myr to diffuse Pb over 25 nm at 800°C and 700°C, respectively (Gardés et al. 2006, 2007; Gardès and Montel, 2009). Evidence for such diffusion-controlled Pb mobility in monazite, activated by a protracted high-temperature thermal event, has been described as 20 nm wide Pb-rich exsolutions (Seydoux-Guillaume et al. 2019). Stress and deformation also enhance fast Pb mobility through crystal-plastic deformation (Fougerouse et al. 2021a, b). In the presence of fluids, elemental mobility is often assumed to be achieved through dissolution-precipitation. This results either in replacement of pre-existing monazite (Grand'Homme et al. 2018) or new growth of minerals (Seydoux-Guillaume et al. 2002). The replacement progresses through the formation of nano-channels (Harlov et al. 2005; Grand'Homme et al. 2018; Budzyń et al. 2021) which act as the loci for mineral-fluid chemical exchange within the mineral. This leads to the creation of further nanoporosity, enhanced fluid infiltration, entrapment of fluid inclusions (Putnis 2002; Harlov et al. 2005, 2007; Putnis et al. 2005; Seydoux-Guillaume et al. 2015; Grand'Homme et al. 2018; Varga et al. 2020; Budzyń et al. 2021), and crystallization of nanoscale phases (Harlov et al. 2005, 2011; Budzyń et al. 2021, 2022).

Several processes promoting Pb mobility at the nanoscale, all with the potential to leave behind nanoscale features (cluster, nanophases) operate within monazite. A variety of such features have been recognized (Seydoux-Guillaume et al. 2003; Fougerouse et al. 2018, 2021 a, b; Turuani et al. 2022) but have not, as yet, been studied systematically in a single sample so that their significance and potential use for nanoscale geochronology can be assed in detail. Hence, the goal of this study is to define and specify the mechanisms and conditions responsible for the formation of nanoscale features in monazite. To do this, isotopically discordant monazite

grains in a paragneiss from Zircon Point in the Archaean Napier Complex of Enderby Land, East Antarctica (Black et al. 1984) have been reinvestigated. Nanophases of galena (PbS) have already been documented in this sample (Turuani et al. 2022) but their mechanisms of formation remain ambiguous. Understanding how monazite interacts with its evolving host rock environment will enable a more robust interpretation of geochemical and isotopic data obtained from complex monazite grains preserved in geological terrains subjected to ancient (~Ga) high-grade polymetamorphic events (e.g. Madagascar; Seydoux-Guillaume et al. 2003).

Geological background

The studied sample is an Archean garnet-rich paragneiss from Zircon Point, located in Casey Bay in the Napier Complex, East Antarctica (Fig. 1a, b). The region underwent a major ultra-high temperature (UHT) event (1050-1120°C, 7-11 kbar) at *ca.* 2.58-2.45 Ga (Harley and Motoyoshi 2000; Hokada et al. 2004; Kelly and Harley 2005; Harley 2016; Clark et al. 2018) accompanied by pervasive deformation of terranes (Fig. 1b) and followed by isobaric cooling (< 800°C; Harley 1985; Harley and Black 1987; Kelly and Harley 2005). Later localized upright mylonitic shear zones (Sheraton et al. 1980; Black et al. 1983a, b, 1987; Sandiford and Wilson 1983; Sandiford 1985) are inferred to be related to the *ca.* 1 Ga Rayner Structural Episode (Kelly et al. 2000, 2002; Halpin et al. 2005; Horie et al. 2016) which also caused spatially focused and variable retrogression of rocks under amphibolite conditions. Localized pegmatites intruded the basement near Zircon Point at *ca.* 0.55 Ga (Sheraton et al. 1980; Black et al. 1983a; Grew et al. 2001).

Monazite crystals from Zircon Point locality have been previously studied in detail (Black et al. 1984; Turuani et al. 2022). They are isotopically discordant on Wetherill and Tera-Wasserburg plots, with U-Th dates spread between 2.43 ±0.02 and 1.09 ±0.03 Ga (ID-TIMS; Black et al. 1984). Monazite initially crystallized at 2.44 ±0.04 Ga as indicated by the upper

intercept of the discordia (LA-ICP-MS; Turuani et al. 2022), during or near the peak of UHT metamorphism in the area (Kelly and Harley 2005; Harley 2016; Clark et al. 2018). The discordance has been attributed to the presence of nanophases that contain inherited Pb* (Turuani et al. 2022). The monazite host that lacks Pb*-bearing nanophases has been dated by atom probe at 1.02 ±0.26 Ga (Turuani et al. 2022), corresponding within error to the lower intercept of the discordia formed by the total monazite dataset, at 1.09-1.05 Ga (ID-TIMS and LA-ICP-MS respectively; Black et al. 1984, Turuani et al. 2022). This age reflects the amphibolite facies retrogression associated with reworking during the Rayner Structural Episode (Black et al., 1983, 1987; Kelly et al. 2000, 2002; Halpin et al. 2005; Horie et al. 2016), which induced resetting of the U-Th-Pb chronometers at the nanoscale in monazite (Turuani et al. 2022). Some Pb*-bearing nanophases have an isotopic signature corresponding to Pb* formed between 2.44 ±0.04 and 1.02 ±0.26 Ga and isolated as nanoreservoirs at *ca.* 1 Ga. Other Pb*-bearing nanophases have an isotopic composition that reflects an isolation as nanoreservoirs at *ca.* 0.55 Ga (Turuani et al. 2022).

Methods

Scanning electron microscopy (SEM); electron probe microanalysis (EPMA) and electron backscatter diffraction (EBSD)

Petrographic features were observed using optical microscopy. Textural features of monazite grains were examined using the scanning electron microscope with field emission gun SEM-FEG Zeiss supra 55vp hosted at the ENS in Lyon (France). The instrument is equipped with energy dispersive X-ray spectroscopy (EDS), secondary electron (SE) and backscattered electron (BSE) detectors.

Electron probe microanalysis (EPMA) has been used for quantitative analyses and chemical mapping was carried out using a CAMECA SXFive hosted at the Micro-characterization center

R. Castaing in Toulouse (France). Quantitative analyses were conducted under analytical conditions of 15 kV and 20 nA. Analytical conditions of 15 kV and 40 nA with a step size of 1 µm were used for chemical mapping of MzA2 and Mnz25. Chemical mapping of Mnz13 was carried out using a CAMECA SXFive FE under condition of 7 kV and 100 nA. Additional analytical details are given in Table S1.

Electron backscatter diffraction analyses (EBSD) were undertaken on Mnz13 using a Tescan Lyra3 focused ion beam (FIB) coupled with a SEM, hosted in the John de Laeter Centre at Curtin University in Perth (Australia). The instrument is equipped with an EBSD detector. Data acquisition was conducted under conditions of 20 kV and 149 µA, with a step size of 0.07 µm, a spot size of 27 nm, a beam intensity of 16 and a working distance of 12.5 mm.

Transmission electron microscopy (TEM)

Five TEM-foils were prepared in three monazite crystals (Mnz25, Mnz4 and Mnz17) using a focused ion beam FIB/SEM Thermo Fisher Scientific FEI Helios Nanolab 600i instrument hosted by MANUTECH USD plateform in Saint-Etienne (France). FIB-foils were observed on a JEOL NeoARM200F Cold FEG-TEM owned by the CLYM (*Consortium Lyon St-Etienne de Microscopie*) and hosted within the Hubert Curien Laboratory in Saint-Etienne. This instrument is fitted with a cold-field emission gun and equipped with the latest generation of spherical aberration corrector on the condenser lenses. It is also equipped with a wide-angle EDS spectrometer SDD CENTURIO-X from JEOL, two scanning detectors (JEOL and Gatan annular dark and bright field-ADF/ABF), and an electron energy-loss spectrometer (EELS, Gatan GIF Quantum ER). Some observations (Fig. 6a, b) have been done on a Jeol2100F hosted at the *Centre Technologique des Microstructures* in Lyon (France). Analyses were operated at 200 kV.

Atom probe tomography (APT)

Eleven atom probe specimens were lifted-out from three monazite crystals (Mnz25, MzA2, Mnz17) and prepared using the Tescan Lyra3 dual Ga^+ FIB/SEM at Curtin University. More detailed process for the lift-out and targeting methods are described in Thompson et al. (2007) and Rickard et al. (2020). Atom probe analyses were conducted at the Geoscience Atom Probe Facility at Curtin University. The Cameca LEAP 4000X HR instrument was set to a base specimen temperature of 60 K and detection rate of 0.01 atoms/pulse (1%). In order to optimize acquisition, field evaporation was controlled by a UV laser (λ=355 nm) pulsed at 125 kHz with a pulse energy of 300 pJ for monazite and 30 pJ for galena. Data processing and reconstruction was performed using Cameca's IVAS v3.8.4 and AP Suite 6 software. Both atomic and molecular ions, with charge states of 1+ to 3+ were identified in the time-of-flight spectrometry mass/charge spectra. For reconstructing the atom probe data an evaporation field of 27.02 V/nm and an atomic average for monazite of 0.01245 nm^3/atom were used following the recommendations of Fougerouse et al. (2022). More details are available in Table S2.

Microscale results

Petrographic description

The studied rock (sample name: 5037) is a garnet-rich migmatitic paragneiss which preserves high-grade layer-parallel fabric defined by both variations in mineral modes and the parallel elongation of ribbon- or lozenge-shaped rutilated quartz grains and ovoid garnet (Black et al. 1983a, 1984). The mineralogy is dominated by rutilated quartz (rt-quartz), ternary feldspar, poikiloblastic garnet and sillimanite (Fig. 1c). Accessory minerals are zircon, rutile and monazite. Garnet (1 mm diameter) contains sporadic rounded inclusions of quartz, sillimanite, primary biotite and finer rutile. Quartz occurs in two textural varieties. Elongate 'ribbon' porphyroblastic quartz may show undulose extinction and is rich in oriented rutile

needles (rt-qz), causing it to be weakly pleochroic in white to very pale brown. Granoblastic quartz occurs in arrays on elongate quartz ribbons, adjacent to garnet, or with feldspar in the matrix. Ternary feldspar is strongly mesoperthitic, characterized by regularly distributed string and filament exsolution types, and all ternary feldspar grains hosts hundreds of small monazite grains about 1-4 μm in diameter. Plagioclase occurs along with K-feldspar in granoblastic grain clusters formed on and replacing former mesoperthite. Plagioclase may also occur as thin (~ 50 μm in width) moats or coronas rimming sillimanite and garnet, locally separating them from groundmass quartz (Fig. 1c). Ti-rich red-brown biotite occurs in some garnet-rich horizons (Fig. 1c), forming a moderate foliation parallel to the elongation of the garnet it rims or fractured garnet that it transects (Fig. 1c). Biotite also occurs as sporadic flakes partially replacing former mesoperthitic feldspar. Both textural settings are consistent with the biotite being a late, post-peak, metamorphic mineral in this rock. The studied monazite grains (Ø > 20 μm) are hosted in sillimanite, garnet or rt-quartz porphyroblasts where they are generally surrounded by cracks, or located in the matrix at grain boundaries in the recrystallized seams and associated to late biotite (Fig. 1c), or in the plagioclase-corona (moat) textures on garnet or sillimanite. Cracks around or radiating from monazite are filled in some cases by Fe-oxides.

Monazite textural features

There is a systematic variation in monazite grain size (30-250 μm) with the smallest grains located in garnet, rt-quartz and sillimanite, and the largest grains located in matrix at grain boundaries in recrystallized seams or associated with the plagioclase coronas (Table S3). All grains, irrespective of host mineral and textural setting, show internal features highlighted by variations of Z-contrast on BSE images and mostly reflecting a chemical control of heavy element (e.g. REE, Th) variations (Fig. 2, Table S3). Monazite crystals (Fig. 2) show growth zoning (Mnz17), oscillatory zoning (Mnz2), a core-rim texture (MzA2) or a core surrounded by several intersecting and overlapping chemical domains forming rims (Mnz16). Thinner or

finer-scale features are also identifiable. These include high Z-contrast (bright) lines on the polished surface principally located in the cores (Mnz16, Mnz4, Mnz22, Mnz25, Mnz12; Fig. 2) but also crossing into rim zones (Mnz4; Fig. 2) and sub-micrometer domains presenting as bright and low Z-contrast (dark) dots on BSE imaging, which correspond to phases of sub-micrometer to nanometer size (Fig. 2). These both later features are described in detail in the next paragraphs.

Bright linear features are visible in low or high Z-contrast cores and form a network (Figs. 2, 3). Two types of linear features are distinguished by their preferential orientations and widths. Thin linear features about 0.1 µm in width and oriented at *ca.* 90 degrees (Mnz12; Figs. 2) or *ca.* 60 degrees to each other form a thin grid pattern (white arrow Fig. 3b). Coarser linear features (Fig. 3a), about 0.5-1 µm in width, are brighter, thicker, and more distinct than the thinnest ones and appear to intersect and/or overlap with the thinnest grid pattern (black arrow Fig. 3b). The coarsest of these, which form a broad network, are wavy, irregular and show additional features such as bifurcations, radial sprays and echelon arrangements (Figs. 2, 3b). The entire network formed by coarse and thin linear features does not correspond to any areas of preferential misorientation of the lattice as indicated by the EBSD maps (Fig. 3f). EBSD maps show misorientations related to late fractures that cross the grain. Variations are related to different crystallographic orientations through the grain, which varies between 0 and 3°.

Bright and dark nanoscale phases on BSE images ($Ø < 500$ nm) are present in all grains, in both core and rim domains (Figs. 2, 3a-d) and in chemically homogeneous grains. The high Z-contrasts phases (bright in BSE) show no relief while the low Z-contrasts ones, which some that may correspond to holes (dark in BSE), show low relief (Fig. 2, 3c). Nanoscale phases can be isolated, forming dark and bright dots, or polyphased. The sizes and amounts of these nanoscale phases, hereafter simply referred to as ‘nanophases’, vary according to the monazite textural setting and the core-rim domain when that is present (Figs. 2, 3b, d, Table S3). Monazite

located in garnet and rt-quartz contain small (Ø < 300 nm) nanophases whereas monazite located in the matrix and plagioclase coronas may contain nanophases that can be up to 1 µm in size. Monazite rims contain smaller nanophases than cores (Fig. 3b, d).

Monazite composition

Monazite analyzed by EPMA (38 grains; Table S4) have LREE(La-Sm)$_2$O$_3$ compositions in the range of 44-67 wt. %, and HREE (Gd, Dy) are consistently low (< 2 wt. %) with Y_2O_3 never exceeding 1 wt. % and often below the detection limit. Compositions are highly variable in ThO_2 (0.7-25 wt. %), SiO_2 (0.3-6.2 wt. %) and PbO (0.3-3 wt. %), moderate in UO_2 (0.2-1 wt. %) and mostly low in CaO (0-2 wt. %) independently of the petrographic position of the grain. Monazite compositions plotted on the simplified ternary diagram (Fig. 4) vary along a vector between ideal monazite (LREEPO_4) and huttonite ($ThSiO_4$) rather than towards cheralite ($CaTh(PO_4)_2$) independently of internal textural features such as core or rim.

Most monazite grains with core/rim textures have Th-enriched rims that have correspondingly elevated Si and Pb and low LREE and P (Figs. S1, S2). This results in the high Z contrast rims on BSE images (e.g. rims of Mnz25 and MzA2; Fig. 2). Exceptions exist, such as Mnz13, which has a lower Th (Fig. 3e) and U, Y, Si, Pb (Fig. S3) content in the rim. On chemical maps, bright spots with elevated Pb are also present (Figs. S1-S3). In Mnz13, Pb enrichments are also spatially correlate with Si, S, Mg, Al and Fe enrichments (Fig. S3). The linear network present in most grains (Table S3) has elevated Th and Si, and low Y, Ce and P compared with their host domains (Figs. 3e, S1-S3).

Nanoscale results

One FIB-foil was prepared in monazite Mnz17 hosted in rt-quartz (FIB4), one in monazite Mnz4 in garnet (FIB5) and three FIB-foils were prepared in Mnz25 located in the matrix (Fig. 2). Two FIB foils were lift out from the core of Mnz25 targeting a large nanophase (FIB1) and

a coarse ramification of the Th-rich network (FIB2) and one FIB foil targeted the rim of Mnz25 (FIB3).

Nanoscale features description

STEM-ADF imaging of Mnz25-FIB2 shows that the Th-rich network has 3-dimensional component and extends in depth within monazite (Fig. 5a). The contrast difference between the monazite and the Th-rich network domain reflects that monazite contains less Th than the network and thus the area of monazite core is slightly darker on STEM-ADF image (Fig. 5a). The linear network appears as a particularly rich Th domain of the monazite.

STEM-ADF imaging of Mnz25-FIB2 (Fig. 5a) highlights the presence of distinct nanoscale features occurring in high (bright) and low (dark) contrast on STEM-ADF images within the monazite and the Th-rich network domains. The size of the nanoscale features varies from 50 nm up to 500 nm in diameter. On STEM-ADF image, nanoscale features are either dark (top right corner; Fig. 5a) or bright (bottom right corner; Fig. 5a), sometimes isolated or often polyphased and composed by a bright and a dark domain (bottom middle; Fig. 5a). Comparing TEM-BF image (Fig. 5b) and STEM-ADF image (Fig. 5c) of one nanophase, the presence in the domain (1) of Bragg diffraction contrasts in TEM-BF image (Fig. 5b) demonstrate the crystalline state of the area, while the bright contrasts on the same domain on STEM-ADF image indicate the presence of high-density material (Fig. 5c). In comparison, the low diffraction contrasts on TEM-BF image (Fig. 5b) in the domain (3) indicate the presence of a very low-crystalline state material (mostly amorphous) while the dark contrasts on the same area (3) on STEM-ADF image indicate the presence of low-density material (Fig. 5c). On TEM-BF image, the monazite domain (2) shows typical mottled diffractions contrasts (Fig. 5b) resulting from a distorted lattice due to the presence of radiation damage in monazite (Seydoux-Guillaume et al., 2004).

Mnz25-FIB3 foil, was obtained from the rim of Mnz25, yields a STEM-ADF image that shows high numbers of nanophases highlighted by bright and dark contrasts (Fig. 5d). The size of the nanophases varies between 50 nm up to 100 nm in diameter. Most of them are polyphased and composed of a crystalline domain containing high-density material (1) and an amorphous domain containing low-density material (2). The crystalline domain (1) appears to be in some cases an agglomerate of nanocrystals.

STEM-ADF images of Mnz17-FIB4 (hosted in rt-quartz) and Mnz4-FIB5 (hosted in garnet) show the presence of very high number of nanophases highlighted by bright and dark contrasts (Figs. 5e, S4). The size of nanophases varies between 20 nm up to 100 nm in diameter. Most of them are polyphased and composed by a crystalline domain (1) containing high-density material (Fig. 5f) and by an amorphous domain (3) containing low-density material (Fig. 5f). The crystalline domain (1) appears to be in some cases polycrystalline (Fig. 5f).

Crystallographic information of nanoscale features

Selected area electron diffraction (SAED) patterns have been obtained in three crystalline nanophases. The three nanophases are located in Mnz25-FIB1 (Fig. 6a) and Mnz4-FIB5 (phase 2 and 3; Figs. 6c, S5). The diffraction patterns allow the measurement of d(hkl) spacings summarized in table 1. One nanophase (Fig. 6a) was large enough (Ø ~ 500 nm) so that the diffraction spots obtained on the diffraction pattern (Fig. 6b) only correspond to the nanophase. The d(hkl) spacings measured on the diffraction pattern (Fig. 6b) of 3.46 Å, 2.94 Å and 1.79 Å agree with the (111), (200) and (311) d-spacings of galena (PbS; 3.43, 2.97 and 1.79 Å respectively; Table 1; Wyckoff 1963) in the [0-20] zone axis. Phase 2 is smaller (crystalline domain Ø ~ 50 nm; Fig. 6c) so the diffraction pattern obtained is composed with diffraction spots corresponding to monazite and phase 2 combined (Fig. 6d). Only the d(hkl) spacings of phase 2 have been measured and correspond to 4.19 Å, 4.00 Å, 3.79 Å and 3.40 Å. These d-spacings cannot be related to galena crystallographic parameters, nor metallic Pb, but could

correspond to the (110 or -110 or -102), (20-1), (101) and (-1-12 or -112) d-spacings of crystalline Pb_2O_3 (4.23, 3.88, 3.79 and 3.38 Å respectively; Table 1; Bouvaist and Weigel 1970). The d(hkl) spacings of 3.06 Å, 2.96 Å, 2.17 Å, 1.77 Å and 1.57 Å measured on diffraction patterns obtained on phase 3 (Fig. S5) do not allow mineral identification but exclude galena and metallic Pb because of the close but distinct d-spacings at 3.06 and 2.96 Å (Table 1).

High resolution nanoscale features identification

Nanoscale features called "clusters" appear in all FIB foils as tiny bright domains in STEM-ADF mode (Fig. 7a). These features have a size always below 10 nm in diameter (Ø ~ 2-5 nm; Fig. 7b, c). High resolution (HR-)STEM-ADF imaging (Fig. 7b, c) reflects arrangement of heavy atoms (e.g. Ce; Fig. 7e) within the monazite structure. Here this organization is not homogeneous within the entire volume (Fig. 7b, c) and demonstrates the presence of heavier atoms (brightest area) within the volume forming the cluster (Fig. 7c). HR-STEM-ADF imaging highlights also an off-center area with darker contrasts that may correspond to the presence of lower density material or possibly to slight Bragg diffraction contrasts variations surrounding the cluster due to the presence of a distorted lattice as shown at lower magnification (Fig. 7a). Fast Fourier transform (FFT; Fig. 7d) of the HR-STEM-ADF image filtered for noise reduction (Fig. 7c) shows diffraction spots from monazite in [001] zone axis. There is no difference in term of crystallography due to the presence of the cluster, and no sharp interface between the monazite host and the cluster (Fig. 7b, c); the lattice remains continuous between clusters and monazite (Fig. 7b-d).

Composition of nanoscale features

EDS with TEM

EDS chemical profiles of the nanophases (Ø ≥ 100 nm) highlighted in Mnz25-FIB2 (Figs. 5b, c, 8a) and Mnz17-FIB4 (Fig. 8b) show that the crystalline parts essentially consist of Pb

(red profiles on spectra; Fig. 8a, b). The black spectrum obtained on the amorphous domain in the nanophase observed in Mnz25-FIB2 (dark contrasts on STEM-ADF image; Fig. 8a) shows that this area contains mostly Si, Mg, Al and Fe. In the nanophase observed in Mnz17-FIB4, the low-crystalline part consists of Fe and S (black spectra; Fig. 8b). The REE, P and Th peaks on black and red spectra reflect mixing with monazite component (grey spectra; Fig. 8a, b) and Cu peak to the grids used to hold FIB foils. Comparing the O/P ratio between monazite (grey spectra) and nanophase (red spectra), it is possible to identify two types of Pb-bearing nanophases (Table S5). The first type (4 observations) shows no O associated with Pb and the second type consists of oxides (3 observations) showing the association of O with Pb in the crystalline part.

An EDS spectrum obtained on a cluster (red) shows elevations in Pb and very slightly in Si coupled with relative depletions in LREE, P and O in comparison to the spectrum obtained on the surrounding monazite (Fig. 9). Ca content is similar in both cluster and monazite host. An EDS chemical map of another cluster shows high concentration of Pb with a slight increase of Ca while Si remains homogeneous (Fig. S6).

APT

The location of eleven tips for APT analysis is shown in figure 2 and figure S7. Specimens were prepared from monazite grains located in the matrix (Mnz25, MzA2) and in rt-quartz (Mnz17) with specific targets in each case. Specimen M16 (Mnz25) targets a thin linear feature of the Th-rich network while M17 and M6 specimens target large nanophases (~ 500 nm) in Mnz25 and MzA2 respectively. Specimens M15, M19, M21 (in Mnz25), M2, M3, M5 (in MzA2) and M3’ (in Mnz17) target homogeneous areas at the microscale in core and rim.

Th isoconcentration surfaces are shown in the reconstruction of specimen M16 (Fig. 10a) and represent points of a threshold value for Th of 0.15 at. % (Hellman et al 2000). The Th-rich feature targeted corresponds in 3D to a plane of 0.1 µm width (Fig. 10a). The increase in Th is

progressive between the monazite host and the feature and Si distribution reconstruction shows higher Si concentrations within the Th-rich feature (Fig. 10a).

The Si distribution reconstruction also highlights the presence of Si-rich nanoscale features forming clumps about 20 nm in diameter (Fig. 10a) that correspond with heterogeneities in Pb. Aluminum heterogeneities are also spatially correlated with that of Si and Pb (Fig. 10a). APT reconstruction of specimen M19 shows the distribution of Pb, Ca, Si, S, Mg and Al which highlights the presence of nanoscale features (Fig. 10b). One shows a size of 30 nm in diameter and high concentration of Mg, Al, Si ±Ca ±Pb. Other reconstructions also highlight the presence of such domains (M22, M21 in Mnz25 and M2, M3 in MzA2; Figs. S8-S11).

Other nanoscale features are observed, showing size variability, some highlighted by S and Pb distributions as in the reconstruction of specimen M6 from MzA2. It shows the interface between the nanophase and monazite. The distribution of Pb and S shows the concentration of these elements at the top of the specimen highlighting the presence of galena (Fig. 10c). Others APT reconstructions highlight correlation between Pb and S concentration and forming smaller (Ø < 50 nm) nanoscale features (M3' in Mnz17, M2 in MzA2 and M17 in Mnz25; Figs. S11-S13).

APT reconstruction of specimen M19 shows that Pb and Ca distributions are heterogeneous and form clumps of ~ 10 nm diameter (Fig. 10b) that are compositionally different from the Pb-Si-Ca-Mg-Al nanoscale features in the same specimen. APT reconstruction of specimen M15 highlights clumps of similar size characterized by heterogeneous Pb and Si distributions (Fig. 11a). A proximity histogram (proxigram) constructed considering three clumps in M15 shows an increase of Pb up to 3.5 at. % coupled with Si up to 4.5 at. %, and a slight increase in Ca of 0.5 at. % compared to monazite matrix composition (Fig. 11b, Tables S6, S7). Forty-four chemical profiles with a binwidth of 1 nm have been performed crossing similar clumps in 9 APT specimens. The clumps considered are all up to 10 nm in size, and exclusively enriched in

Pb ±Si ±Ca. Three chemical groups can be highlighted related to composition: one with Pb associated with Si (Pb-Si group), another where Pb is associated with Ca (Pb-Ca group), and a third in which Pb is associated with both Ca and Si (Pb-Si-Ca group). Data from Pb-Si-Ca and Pb-Si groups broadly plot long a 1:1 line on Pb *vs* Ca + Si diagram (Fig. 11c) with a slope of the trend lines of 1 and 0.77 respectively. Pb-Ca group data broadly plot along a 1:2 line forming a line with a slope of 0.49 (Fig. 11c).

Discussion

Formation of Th-rich network through fluid pathways

The presence of a Th-rich network, whose features have been synthetized table 2, is not related to the textural position of the monazite grain, nor to the ThO_2 content of the monazite itself. Monazite grains containing *ca.* 30 wt % of ThO_2 have been reported but not noted, on the basis of the imaging available at the time, as having such features (Della Ventura et al. 1996; Lumpkin 1998). The intersections at angles of 60 degrees in Mnz13 (Fig. 3b) but also at 90 degrees in Mnz12 (Fig. 2) may correspond to angles of monazite crystallographic planes and hence suggests a crystallographic control. For example, according to the crystallographic parameters of Ni et al. (1995), (010)^(001) = (010)^(100) = 90°, (-111)^(001) = 58°, (-101)^(011)=61°, (111)^(010) = 59° or (111)^(1-11) = 60°. Diffusional pathways controlled by twin formation have been highlighted in monazite which underwent crystal-plastic deformation (Fougerouse et al. 2021b). However, in the absence of stress and at usual crustal temperatures (< 800°C), volume-diffusion of Th is too slow (3 orders of magnitude slower than Pb diffusion) to form Th-rich exsolutions lamellae (Cherniak et al. 2004; Gardés et al. 2006).

Chemical reaction promoted through mineral-fluid interaction is one of the most efficient mechanism to facilitate element mobility in monazite (Seydoux-Guillaume et al. 2002) and experimental studies have highlighted Th enrichments at the interface between primary and

secondary monazite (Seydoux-Guillaume et al. 2002; Harlov et al. 2011). Bright, Th-enriched lines have been interpreted as healed and sealed fractures that could have acted as channels for fluids (Kelly et al. 2012). However, in the present example, the Th-rich features form a fine mesh or network showing a crystallographic control that does not conform to any pattern expected of sealed fractures. Therefore, the intriguing Th-rich networks preserved in the monazite grains are interpreted as inherited traces of largely crystallographically-controlled (or moderated) fluid pathways through the mineral. Such alteration proceeding along crystallographic orientation has been observed in experimentally altered monazite (Budzyń et al. 2015, 2021). In the present study, it may correspond to inherited traces of high residual stress in the grains, which then represent preferential sites for fluid exchanges and dissolution (e.g. in halite; Bosworth 1981 or in quartz; Blum et al. 1990). The presence in the Th-rich network of nanoscale features containing Al (Fig. 10a), which cannot be incorporated in the monazite lattice and must come from and external source (i.e. fluid), also argues for this interpretation.

Pb* accommodation in monazite

The $^{207}Pb/^{206}Pb$ isotopic quantification of clusters with APT was not successful due to the low $^{207}Pb^{+}$ counts and the overlap between $^{207}Pb^{2+}$ and $ThPO_3^{3+}$. Whilst a previous study on natural monazite was able to temporally constrain Pb-rich anhydrite clusters formation using $^{208}Pb/^{206}Pb$ ratios (Seydoux-Guillaume et al. 2019), in the present study the isotopic results obtained using the same approach are subject to high uncertainties and hence are not considered reliable for age estimation. Given the lack of a reliable age estimate for the timing of cluster formation other timing criteria are required and several hypotheses have been explored. First, clusters could be heterogeneous growth features formed during monazite crystallisation at UHT conditions. However, SIMS isotopic analysis show that no common Pb is present in monazite (Turuani et al. 2022) and therefore clusters are composed entirely of Pb* derived from the monazite itself, which essentially rules out a formation during early crystallisation. Second,

clusters could be the result of Th and U heterogeneous distribution within the crystallographic lattice (as cheralite or huttonite substitution). If cluster formation was related to primary heterogeneous Th and U contents, a trace of these primary chemical heterogeneities should remain today, given the first order radioactive decay equation and equivalent timespan of decay. However, the measured Th and U contents are similar in the monazite matrix and clusters (Fig. 11b). Having discounted these possibilities, it appears that cluster formation can only be related to secondary Pb*, Ca and Si mobility.

In monazite lattice, the radioactive decay of Th^{4+} or U^{4+} (stage I; Fig. 12) into Pb^{2+} induces a charge deficit that implies a time-dependent charge imbalance within the lattice. This charge deficit may be compensated by the development of vacancies leading to a slight distortion of the lattice to reach electrostatic equilibrium (off-centre darker area on STEM-ADF images; Fig. 7, Table 2). Moreover, the large ionic radius of Pb^{2+} (Shannon 1976) may cause Pb* to be sited in these defects (stage II; Fig. 12). Indeed, clusters are essentially composed of Pb* with sometimes ± Ca and Si (Table 2) that may site not exactly with Pb but slightly spatially offset (off-centre darker area on STEM-ADF images; Fig. 7). Enrichments and accumulation of these elements in vacancies may be facilitate by the recoil nuclei associated with radioactive decay that induce destruction of the lattice and favor diffusion and element mobility over few nanometers (~10 nm; stage I and II; Fig. 12). Charge imbalanced in monazite lattice is induced by the radioactive decay of U^{4+} and Th^{4+} initially incorporate by coupled substitutions with Si^{4+} and Ca^{2+}. These latter elements may thus accommodate as interstitials in the distorted monazite lattice. A positive correlation is observed between Pb*, Si and Ca contents (Fig. 11c) suggesting that Ca and Si in the clusters correspond to the Ca and Si initially associated with U and Th reflecting the huttonite ($Th^{4+}/U^{4+} + Si^{4+} = P^{5+} + REE^{3+}$) and cheralite ($Th^{4+}/ U^{4+} + Ca^{2+} = 2REE^{3+}$) substitutions.

Antagonistic and synchronous mechanism of α-healing induced by U and Th radioactive decay in phosphates limits and prevents grain-scale mobility by restoring the lattice and leads to the freezing of Pb-Ca-Si clusters. Therefore, clusters form by diffusion and preferential segregation of Pb*, Ca and Si in defect sites in response to lattice energy minimization. Repetition of this process over time leads to increase of Pb*, Ca and Si content in clusters that are stabilized by continuous recovery mechanism of the lattice induced by the α-self healing mechanism (Seydoux-Guillaume et al. 2018; stage II; Fig. 12). Clusters are localized in monazite dated at 1.02 Ga (Turuani et al. 2022). This time scale of billion-year might be a prerequisite for clusters formation (see next section). Finally, the mechanism of formation of the clusters only depends on intrinsic monazite parameters and not on external conditions.

Monazite replacement mechanism

Previous work on this sample documented that the Pb*-bearing nanophases carry a $^{207}Pb/^{206}Pb$ ratio compatible with their derivation from the Pb* accumulated in the host monazite crystal between its crystallization (2.44 Ga) and two metamorphic events (at 1.02 and 0.55 Ga; Turuani et al. 2022). At the nanoscale, the monazite matrix yields an average $^{208}Pb/^{232}Th$ age of *ca.* 1.02 Ga while at the grain scale, U-Pb geochronological data obtained in monazite grains hosted in garnet and rt-quartz show a Pb*-loss trend between 2.44 and 1.02 Ga demonstrating that Pb*-bearing nanophases formation and Pb* mobility both at nano and micro-scale occurred at that time and were synchronous (Turuani et al. 2022). Very local nanodomains (10^4 nm^3) yielding ages close to the 0.55 Ga event (Turuani et al. 2022), and broad Pb^*-loss trend in monazite grains hosted in the matrix (more exposed to fluid interactions), both indicate a second Pb* mobility at that time.

Experimental studies of monazite replacement by dissolution-precipitation at 750°C in high Ca and Na-Ca environments have reported nanophases of high-density material within the monazite (Budzyń et al. 2021). In the same study, the experiments done at 550°C indicated that

nanoscale porosity could be created in replaced monazite. In the present study, all monazite grains contain Pb*-bearing nanophases and Si ±Mg ±Fe ±Al amorphous material. Except Si, the latter elements cannot be incorporated in the monazite crystallographic lattice (Clavier et al. 2011). These silicate phases must, therefore, either be generated from an external source such as infiltrating fluid or be representative of primary silicate inclusions trapped during the monazite crystallization at *ca.* 2.44 Ga and subsequently modified. The total monazite matrix resetting at *ca.* 1.02 Ga at the nanoscale (Turuani et al. 2022) and the presence of these silicate phases are best interpreted as remnant of pervasive fluid flow through the crystal (stage III; Fig. 12). This hypothesis of fluid-interaction is further supported by the petrographic observation of secondary biotite on garnet that reflect fluid infiltration at *ca.* 1.02 Ga corresponding to amphibolite facies overprinting event at Zircon Point (Black et al. 1983a, 1987).

Experimental studies alluded to above indicate that monazite alteration by alkali-bearing fluid under amphibolite conditions (500-700 °C) may be under-detected at the microscale using SEM imaging or EPMA analysis, conserving initial features and chemistry, whereas at the nanoscale it can result in complex heterogeneities of crystallised nanophases and trapped nanoscale porosity (Grand'Homme et al. 2018; Budzyń et al. 2021). Thus, in the present study, the compositional zoning observed at the microscale does not necessarily reflect 1.02 Ga domains (e.g. rims) superimposed on inherited 2.44 Ga domains (e.g. cores). Instead, the microscale compositional zoning, such as Th-rich rims on Th-poorer cores, may correspond to fossilised primary textural heterogeneities that reflect several stages of growth and melt interaction (Kelly et al. 2012) at *ca.* 2.44 Ga. The correlation of microscale core-rim chemical and textural differences with different orogenic cycles in that case would be erroneous.

Formation of Pb*-bearing nanophases

In agreement with Black et al. (1984) we infer that at *ca.* 1.02 Ga, garnet and rt-quartz shielded monazite experienced less fluid interactions compared to unshielded monazite in the

quartzo-feldspathic matrix. Pb* formed within the monazite between 2.44 and 1.02 Ga was mobilized by fluid, with several results depending on the amount of fluid accessing the individual grains. The low amount of fluid in the shielded garnet and rt-quartz hosted monazite induced rapid Pb* saturation which induce precipitation of Pb*-bearing nanophases at the replacement reaction front within the monazite (stage IV; Fig. 12), limiting Pb*-leaching and thus Pb*-loss from the grain (Turuani et al. 2022). In contrast, we propose that monazite grains in the quartzo-feldspathic matrix were exposed to greater fluid flux, so that the grain-specific integrated fluid-mineral ratios were also higher. Pb* saturation in the fluid in this case would be retarded, facilitating greater Pb*-loss from the grain (Turuani et al. 2022). When the fluid reached saturation, it likely induced precipitation of bigger Pb*-bearing nanophases (Ø ~ 500 nm). The Pb* contents accumulated in monazite will also affect the amount of Pb*-bearing nanophases. High Pb* content domains (e.g. Mnz25 rim) will favour the precipitation of higher amount of Pb*-bearing nanophases than domains with low Pb* content (e.g. Mnz25 core). Thus, the difference of amounts and sizes of Pb*-bearing nanophases within grains located in garnet and rt-quartz with those located in the matrix can be interpreted in terms of fluid access and ingress, i.e. the microscale extent of fluid-mineral interaction, conditioned by the Pb* content available in the individual monazite grain or domain at the time of fluid-interaction. The low fluid/rock ratio during the retrograde evolution of the rock is supported by the preservation of UHT paragenesis (Black et al. 1983a) and in particular by textures such as the preservation of filamentous mesoperthitic feldspar which lacks microporosity and coarsened and disrupted exsolution lamellae (Parsons and Brown, 1984; Brown and Parsons, 1989; Walker et al. 1995; Hokada, 2001). This low fluid/mineral ratio favored fluid saturation and thus Pb*-bearing nanophase precipitation. A second factor highlights by experimental studies is temperature. Fluid interactions in high temperatures conditions (~700°C) will induce efficient replacement and resetting of monazite and thus effective Pb* mobilization by fluid, while at

lower temperatures (~500°C) kinetics are slower resulting in local replacement and therefore low Pb* mobilization (Grand'Homme et al. 2016).

Sulphur content as limiting factor

The precipitation of galena is not only reliant on the quantity of Pb* present in the monazite at the time of fluid ingress, but also on the availability of S, incorporated in monazite via the coupled substitution $Ca^{2+} + S^{6+} = REE^{3+} + P^{5+}$ (Chakhmouradian and Mitchell 1999). If the fluid-triggered element mobility is commensurate with the scales of the nanophases then the S available in the monazite will act as a limit on the formation of galena (and other S-bearing nanophases associated as FeS). To test this essentially closed-system model, calculations have been performed to evaluate the volumes, and hence radii, of the host monazite domains required to produce a galena nanophase with a range of diameters from 0.1 to 1 micron. As the S content of the pristine monazite prior to galena formation cannot be measured directly, we have used values of 600-400 ppm S for the initial monazite here, typical of many natural monazites that record sulphide breakdown during partial melting (Laurent et al. 2016). Based on these assumed values, the S-depletion region in the host monazite that is required to form a 0.5 μm diameter galena nanophase is 3-4 μm in diameter. This calculation is in good agreement with BSE observations that show a spacing of slightly less than 3-4 μm between 0.5 μm diameter Pb*-bearing nanophases (e.g. Fig. 3b). The spacing would be larger if the initial monazite S is lower. It is also apparent that Pb*-oxides have precipitated where S has been fully depleted. We conclude that for these monazite grains with appreciable Pb* at the time of fluid interaction, the formation of the sulphide (galena and FeS) is most likely limited by S availability from the host monazite.

Prerequisites to Pb*-bearing nanophases formation

A prerequisite for the precipitation of Pb*-bearing nanophases would be the presence of Pb* clusters within monazite lattice. The presence of clusters during monazite-fluids

interactions and the replacement process may induce rapid fluid saturation in Pb* because they represent high content of Pb* easily mobilizable which then induces precipitation of the nanophases (stage III and IV; Fig. 12). In this scenario the formation of Pb*-bearing nanophases would be favored not only by a low fluid/mineral ratio but also by the presence of pre-existing clusters with enhanced Pb* in monazite that was older than 1 Ga at the time of fluid interaction. This age-related effect could explain the principal difference between the monazite studied here and in the experiments of Budzyń et al. (2021), in which nanophases are observed, and that experimentally studied by Grand'Homme et al. (2018), in which only silicate inclusions were observed. The age will affect the Pb* content in monazite at the time of fluid-interaction, and can be assimilated to the α-dose accumulated over time in the lattice (Seydoux-Guillaume et al. 2004). For example, monazite grains in 5037 (1.42 Gyr at the time of first fluid interactions) and from Budzyn et al. (2021; ~1.1 Gyr) would accumulate an α-dose of a least ~10^{20} α/g whilst the monazite studied by Grand'Homme et al. (2016, 2018; ~500 Myr) would accumulate an α-dose ~10^{19} α/g. The latter α-dose of ~10^{20} α/g may represent a threshold lower limit for the formation of sufficiently Pb*-rich clusters in monazite.

Pb* mobility in monazite: geochronological implications

Turuani et al. (2022) have demonstrated that Pb* mobility in these monazite grains induced isotopic disequilibrium and thereby leads to discordant U-Pb isotopic ratios. Both the Pb*-bearing nanophases (galena and oxides) and the clusters highlighted in the present study (Table 2) reflect Pb* mobility in monazite through different mechanisms. Clusters formation is controlled by intrinsic parameters and would be detectable in ancient monazite grains (billions of years old monazite crystals). They may also be favored by high primary U and Th contents in monazite thus leading to high Pb* content. They represent defects where Pb* segregate and accumulate overtime. The geochronological consequences of clusters formation are minor

unless the clusters act as preferential sites of later Pb* loss stimulated by the superposition of subsequent high-T metamorphic or lower to high-T fluid infiltration events.

In contrast, the formation of Pb*-bearing nanophases is controlled by external variables such as temperature, fluid composition and the amount of reactive fluid ingress, which in turn may be controlled by the shielding effect of the mineral in which the monazite is hosted. Intrinsic parameters will then influence the composition of the Pb*-bearing nanophases produced, for example S availability in monazite to form galena. In the studied example, the Pb* formed within monazite between *ca.* 2.44 and *ca.* 1.02 Ga was firstly mobilized by fluids and precipitates in the form of galena or Pb*-oxides when fluid reaches Pb* saturation, in a situation likely favored by very low fluid/monazite ratios and amphibolite conditions related to the known metamorphism event that affect Zircon Point at that time (Black et al. 1983). The Pb*-loss trend measured in these monazite grains (Black et al. 1984; Turuani et al. 2022) is related to the mixing within the analytical volume of conventional dating methods (e.g. EMP, LA-ICP-MS, SIMS) of the 1.02 ±0.26 Ga monazite matrix (APT) and variable amounts of Pb*-bearing nanophases that preserve the isotopic information of the 2.44 ±0.04 Ga event (Turuani et al. 2022). This mixing is shown by *in-situ* isotopic data and by the discordia obtained in monazite grains hosted in garnet and rt-quartz which indicates upper and lower intercepts at 2.44 ±0.04 and 1.05 ±0.13 Ga respectively (Turuani et al. 2022). Monazite grains located in the matrix show a broader dispersion of the discordant U-Pb data, difficult to interpret in isolation (Turuani et al. 2022). This dispersion has been interpreted as related to a second Pb* mobility at *ca.* 0.55 Ga during pegmatite intrusions in Zircon Point (Sheraton et al. 1980; Black et al. 1983a; Grew et al. 2001), highlighted only as a result of the nanoscale investigations (Turuani et al. 2022). This reflects the very localized resetting of the monazite matrix at the nanoscale (stage IV bis; Fig. 12; Turuani et al. 2022) due to lower grade metamorphic conditions (Fig.

S14). Pb*-bearing nanophases formed during this later event record a mixed isotopic signature (Turuani et al. 2022).

Such isotopic dispersion can be completely invisible due to the mixing of many grains (Black et al. 1984) or unnoticed and misinterpreted as analytical errors whereas it actually reflects the record of geological events preserved in the geochronometer (Turuani et al. 2022). Depending on the external conditions, such as temperature, fluid/rock ratio or fluid access, and intrinsic conditions such as the presence of earlier-formed clusters, Pb* mobilization and monazite resetting can be very localized at the nanoscale. Consequentially, nanoscale geochronological investigations are essential in order to develop accurate age interpretations for monazites that have undergone complex geological histories in polymetamorphic terranes.

Conclusions

This study provides evidence for element mobility in monazite which may occur through different mechanisms, resulting in various textural nanoscale features that can impact significantly the use of monazite as geochronometer and the interpretation of isotopic discordance. Th-rich networks appear related to crystallographically-constrained fluid ingress into monazite at low integrated fluid/mineral ratios. Clusters less than 10 nm in size and rich in Pb* ±Si ±Ca appear to form as a consequence of transient radiation damage, which allows the highly localized accommodation of elements in the subsequently annealed but distorted lattice. Pb*-bearing nanophases (galena and oxides) form as a consequence of later fluid ingress within monazite, which caused monazite replacement through dissolution-precipitation combined with the precipitation of nanophases. The mineralogy of Pb*-bearing nanophases is dependent on the microscale availability of elements in the immediate environment of the nanophase, with S in monazite in particular being a limiting factor in the formation of galena. As whole monazite grains are affected by pervasive fluid interaction/reaction (Turuani et al. 2022) the

compositional zoning observed at the microscale does not document secondary monazite alteration but is vestigial, reflecting preserved chemical microscale heterogeneities. The precipitation of Pb*-bearing nanophases within the monazite without extensive modification of the primary chemistry on the grain scale has allowed the age of initial crystallization at 2.44 Ga to be preserved (Turuani et al. 2022). Garnet and especially rutilated quartz (rt-quartz) have shielded monazite grains and therefore, limited fluid access to those monazites, inducing a higher density of Pb*-bearing nanophases in them than in monazites hosted in the fluid-accessible quartzo-feldspathic matrix. The more Pb* precipitates within monazite crystals as Pb*-bearing nanophases, the less potential there is for Pb* loss from monazite at the grain scale when a second high-grade metamorphic event is superimposed on a much older event in which the monazite initially crystallized.

Finally, this study provides new insights for interpretations of dispersed isotopic data. Discordant isotopic datasets may actually provide a record of the effects of several geological events and nanoscale studies are then required to unveil the cryptic signatures of those events. Indeed, in this sample, only nanoscale results have been able to provide evidences to identify the record of the 0.55 Ga event in the geochronometer (Turuani et al. 2022) and hence to correctly interpret the dispersion in the dataset obtained from several monazite grains. Nanoscale investigations therefore appear to be essential in order to elucidate and interpret disturbed geochronometer data, especially in complex ancient (~Ga) polymetamorphic contexts (e.g. Seydoux-Guillaume et al. 2003, Paquette et al. 2004).

Acknowledgements

We thank C. Fellah for her technical assistance with SEM. UJM and CNRS (INSU TelluS-SYSTER and IEA nanomobility) are thanked for financial support and CAMECA for access to Ivas software. We thank the CLYM for access to the TEM in Saint-Etienne (France). We would

like to thank editor Daniela Rubatto and reviewers Bartosz Budzyń and Alfons Berger for their constructive remarks.

References

Black LP, James PR, Harley SL (1983a) Geochronology and geological evolution of metamorphic rocks in the Field Islands area, East Antarctica. J Metamorph Geol 1:277–303. https://doi.org/10.1111/j.1525-1314.1983.tb00276.x

Black LP, James PR, Harley SL (1983b) The geochronology, structure and metamorphism of early Archaean rocks at Fyfe Hills, Enderby Land, Antarctica. Precambrian Res 21:197–222

Black LP, Fitzgerald JD, Harley SL (1984) Pb isotopic composition, colour, and microstructure of monazites from a polymetamorphic rock in Antarctica. Contrib to Mineral Petrol 85:141–148

Black LP, Harley SL, Sun SS, McCulloch MT (1987) The Rayner Complex of East Antarctica: complex isotopic systematics within a Proterozoic mobile belt. J Metamorph Geol 5:1–26. https://doi.org/10.1111/j.1525-1314.1987.tb00366.x

Blum AE, Yund RA, Lasaga AC (1990) The effect of dislocation density on the dissolution rate of quartz. Geochim Cosmochim Acta, 54:283-297. https://doi.org/10.1016/0016-7037(90)90318-F

Boher P, Garnier P, Gavarri JR et al (1985) Monoxyde quadratique PbOα (I): Description de la transition structurale ferro-élastique. J. Solid State Chem. 3 :343-350. https://doi.org/10.1016/0022-4596(85)90197-5

Bolzan AA, Fong C, Kennedy BJ et al (1997) Structural studies of rutile-type metal dioxides. Acta Crystallogr. Sect B 53:373-380. https://doi.org/10.1107/S0108768197001468

Bosworth W (1981) Strain-induced preferential dissolution of halite. Tectonophysics 78:509-525. https://doi.org/10.1016/0040-1951(81)90026-3

Bouvaist J, Weigel D (1970) Sesquioxyde de plomb, Pb2O3. I. Determination de la structure. Acta Crystallogr. Sect A 26:501–510. https://doi.org/10.1107/S0567739470001316

Budzyń B, Konečný P and Kozub-Budzyń GA (2015) Stability of monazite and disturbance of the Th-U-Pb system under experimental conditions of 250-350°C and 200-400 MPa: Annales Societatis Geologorum Poloniae, v.85, p. 405-424. https://doi.org/10.14241/asgp.2015.016

Budzyń B, Wirth R, Sláma J, et al (2021) LA-ICPMS, TEM and Raman study of radiation damage, fluid-induced alteration and disturbance of U-Pb and Th-Pb ages in experimentally metasomatised monazite. Chem Geol 583:. https://doi.org/10.1016/j.chemgeo.2021.120464

Budzyń B, Wirth R, Sláma J, et al (2022) A detailed and comprehensive TEM, EPMA and Raman characterization of high-metamorphic grade monazites and their U-Th-Pb systematics (the Góry Sowie Block, SW Poland). Chem Geol 607:. https://doi.org/10.1016/j.chemgeo.2022.121015

Budzyń B, Wirth R, Sláma J et al (2023) Atomic-scale Th and U segregation into dislocation cores and U-Pb age discordance in xenotime. Lithos. https://doi.org/10.1016/j.lithos.2023.107105

Černok A, White LF, Anand M, et al (2021) Lunar samples record an impact 4.2 billion years ago that may have formed the Serenitatis Basin. Commun Earth Environ 2:1–9. https://doi.org/10.1038/s43247-021-00181-z

Chakhmouradian AR, Mitchell RH (1999) Niobian ilmenite, hydroxylapatite and sulfatian alternative hosts for incompatible in calcite elements. Can Mineral 37:1177–1189

Cherniak DJ, Watson EB, Grove M, Harrison TM (2004) Pb diffusion in monazite: A combined RBS/SIMS study. Geochim Cosmochim Acta 68:829–840. https://doi.org/10.1016/j.gca.2003.07.012

Clark C, Taylor RJM, Kylander-Clark ARC, Hacker BR (2018) Prolonged (>100 Ma) ultrahigh temperature metamorphism in the Napier Complex, East Antarctica: A petrochronological investigation of Earth's hottest crust

Clavier N, Podor R, Dacheux N (2011) Crystal chemistry of the monazite structure. J Eur Ceram Soc 31:941–976. https://doi.org/10.1016/j.jeurceramsoc.2010.12.019

Della Ventura G, Mottana A, Parodi GC, et al (1996) Monazite-huttonite solid-solutions from the Vico Volcanic Complex, Latium, Italy. Mineral Mag 60:751–758. https://doi.org/10.1180/minmag.1996.060.402.04

Fougerouse D, Reddy SM, Saxey DW, et al (2018) Nanoscale distribution of Pb in monazite revealed by atom probe microscopy. Chem Geol 479:251–258. https://doi.org/10.1016/j.chemgeo.2018.01.020

Fougerouse D, Cavosie AJ, Erickson T, et al (2021a) A new method for dating impact events-Thermal dependency on nanoscale Pb mobility in monazite shock twins. Geochim Cosmochim Acta 314:381–396. https://doi.org/10.1016/j.gca.2021.08.025

Fougerouse D, Reddy SM, Seydoux-Guillaume A, et al (2021b) Mechanical twinning of monazite expels radiogenic lead. Geology 49:417–421. https://doi.org/https://doi.org/10.1130/G48400.1

Fougerouse, Saxey D, Rickard W, et al (2022) Standardizing Spatial Reconstruction Parameters for the Atom Probe Analysis of Common Minerals. Microsc Microanal 28:1221–1230. https://doi.org/10.1017/S1431927621013714

Gardés E, Jaoul O, Montel JM, et al (2006) Pb diffusion in monazite: An experimental study of Pb2 ++ Th4 +⇔ 2 Nd3 +interdiffusion. Geochim Cosmochim Acta 70:2325–2336. https://doi.org/10.1016/j.gca.2006.01.018

Gardés E, Montel JM, Seydoux-Guillaume AM, Wirth R (2007) Pb diffusion in monazite: New constraints from the experimental study of Pb2 + ⇔ Ca2 + interdiffusion. Geochim Cosmochim Acta 71:4036–4043. https://doi.org/10.1016/j.gca.2007.06.036

Grand'Homme A, Janots E, Seydoux-Guillaume AM, et al (2018) Mass transport and fractionation during monazite alteration by anisotropic replacement. Chem Geol 484:51–68. https://doi.org/10.1016/j.chemgeo.2017.10.008

Grew ES, Suzuki K, Asami M (2001) CHIME ages of xenotime, monazite and zircon from beryllium pegmetites in the Napier Complex, Khmara Bay, Enderby Land, East Antarctica. Polar Geosci 14:99–118

Halpin JA, Gerakiteys CL, Clarke GL, et al (2005) In-situ U-Pb geochronology and Hf isotope analyses of the Rayner Complex, east Antarctica. Contrib to Mineral Petrol 148:689–706. https://doi.org/10.1007/s00410-004-0627-6

Harley SL (1985) Garnet-orthopyroxene bearing granulites from enderby land, Antarctica: Metamorphic pressure temperature-time evolution of the archaean napier complex. J Petrol 26:819–856. https://doi.org/10.1093/petrology/26.4.819

Harley SL (2016) A matter of time: The importance of the duration of UHT metamorphism. J Mineral Petrol Sci 111:50–72. https://doi.org/10.2465/jmps.160128

Harley SL, Black LP (1987) The Archaean geological evolution of Enderby Land , Antarctica Geological setting and summary of features The first recognized deformation event in the. 285–296

Harley SL, Motoyoshi Y (2000) Al zoning in orthopyroxene in a sapphirine quartzite: Evidence for >1120 °C UHT metamorphism in the Napier Complex, Antarctica, and implications for the entropy of sapphirine. Contrib to Mineral Petrol 138:293–307. https://doi.org/10.1007/s004100050564

Harlov DE, Wirth R, Förster HJ (2005) An experimental study of dissolution-reprecipitation in fluorapatite: Fluid infiltration and the formation of monazite. Contrib to Mineral Petrol 150:268–286. https://doi.org/10.1007/s00410-005-0017-8

Harlov DE, Wirth R, Hetherington CJ (2007) The relative stability of monazite and huttonite at 300-900 °C and 200-1000 MPa: Metasomatism and the propagation of metastable mineral phases. Am Mineral 92:1652–1664. https://doi.org/10.2138/am.2007.2459

Harlov DE, Wirth R, Hetherington CJ (2011) Fluid-mediated partial alteration in monazite: The role of coupled dissolution-reprecipitation in element redistribution and mass transfer. Contrib to Mineral Petrol 162:329–348. https://doi.org/10.1007/s00410-010-0599-7

Hill RJ (1985) Refinement of the structure of orthorhombic PbO (massicot) by Rietveld analyses of neutron powder diffraction data. Acta Cryst. C41 9:1281-1284. https://doi.org/10.1107/S0108270185007454

Hokada T, Misawa K, Yokoyama K, et al (2004) SHRIMP and electron micropobe chronology of UHT metamorphism in the Napier Complex, East Antarctica: Implications for zircon growth at >1,000 °C. Contrib to Mineral Petrol 147:1–20. https://doi.org/10.1007/s00410-003-0550-2

Horie K, Hokada T, Motoyoshi Y, et al (2016) U–Pb zircon geochronology in the western part of the Rayner Complex, East Antarctica. J Mineral Petrol Sci 111:104–117. https://doi.org/10.2465/jmps.150811

Joseph C, Fougerouse D, Saxey DW et al (2021) Xenotime at the Nanoscale: U-Pb Geochronology and Optimisation of Analyses by Atom Probe Tomography. Geostand Geoanal Res 45(3), 443-456. https://doi.org/10.1111/ggr.12398

Kelly NM, Clarke GL, Carson CJ, White RW (2000) Thrusting in the lower crust: Evidence from the Oygarden Islands, Kemp Land, East Antarctica. Geol Mag 137:219–234. https://doi.org/10.1017/S0016756800004027

Kelly NM, Clarke GL, Fanning CM (2002) A two-stage evolution of the Neoproterozoic Rayner Structural Episode: New U-Pb sensitive high resolution ion microprobe constraints from the Oygarden Group, Kemp Land, East Antarctica. Precambrian Res 116:307–330. https://doi.org/10.1016/S0301-9268(02)00028-1

Kelly NM, Harley SL (2005) An integrated microtextural and chemical approach to zircon geochronology: Refining the Archaean history of the Napier Complex, east Antarctica. Contrib to Mineral Petrol 149:57–84. https://doi.org/10.1007/s00410-004-0635-6

Kelly NM, Harley SL, Möller A (2012) Complexity in the behavior and recrystallization of monazite during high-T metamorphism and fluid infiltration. Chem Geol 322–323:192–208. https://doi.org/10.1016/j.chemgeo.2012.07.001

Kusiak MA, Whitehouse MJ, Wilde SA, et al (2013) Mobilization of radiogenic Pb in zircon revealed by ion imaging: Implications for early Earth geochronology. Geology 41:291–294. https://doi.org/10.1130/G33920.1

Kusiak MA, Dunkley DJ, Wirth R, et al (2015) Metallic lead nanospheres discovered in ancient zircons. Proc Natl Acad Sci 112:4958–4963. https://doi.org/10.1073/pnas.1415264112

Kusiak MA, Kovaleva E, Wirth R, et al (2019) Lead oxide nanospheres in seismically deformed zircon grains. Geochim Cosmochim Acta. https://doi.org/10.1016/j.gca.2019.07.026

Laurent AT, Seydoux-Guillaume AM, Duchene S, et al (2016) Sulphate incorporation in monazite lattice and dating the cycle of sulphur in metamorphic belts. Contrib to Mineral Petrol 171:. https://doi.org/10.1007/s00410-016-1301-5

Lumpkin GR (1998) Rare-element mineralogy and internal evolution of the Rutherford #2 pegmatite, Amelia County, Virginia: A classic locality revisited. Can Mineral 36:339–353

Ni Y, Hughes JM, Mariano AN (1995) Crystal chemistry of the monazite and xenotime structures. Am Mineral 80:21–26. https://doi.org/0003-004X/95/0102-0021

Paquette JL, Goncalves P, Devouard B, Nicollet C (2004) Micro-drilling ID-TIMS U-PB dating of single monazites: A new method to unravel complex poly-metamorphic evolutions. Application to the UHT granulites of Andriamena (North-Central Madagascar). Contrib to Mineral Petrol 147:110-122. https://doi.org/10.1007/s00410-003-0549-8

Peterman EM, Reddy SM, Saxey DW, et al (2016) Nanogeochronology of discordant zircon measured by atom probe microscopy of Pb-enriched dislocation loops. Sci Adv 2:. https://doi.org/10.1126/sciadv.1601318

Peterman EM, Reddy SM, Saxey DW, et al (2019) Nanoscale processes of trace element mobility in metamorphosed zircon. Contrib to Mineral Petrol 174:. https://doi.org/10.1007/s00410-019-1631-1

Peterman EM, Reddy SM, Saxey DW, et al (2021) Trace-element segregation to dislocation loops in experimentally heated zircon. Am Mineral 106:1971–1979. https://doi.org/10.2138/am-2021-7654

Piazolo S, La Fontaine A, Trimby P, et al (2016) Deformation-induced trace element redistribution in zircon revealed using atom probe tomography. Nat Commun 7:1–7. https://doi.org/10.1038/ncomms10490

Putnis A (2002) Mineral replacement reactions: from macroscopic observations to microscopic mechanisms. Mineral Mag 66:689–708. https://doi.org/10.1180/0026461026650056

Putnis C V., Tsukamoto K, Nishimura Y (2005) Direct observations of pseudomorphism: Compositional and textural evolution at a fluid-solid interface. Am Mineral 90:1909–1912. https://doi.org/10.2138/am.2005.1990

Sandiford M (1985) The origin of retrograde shear zones in the Napier Complex; implications. Mult Deform ductile brittle rocks 7:477–488

Sandiford M, Wilson CJL (1983) The geology of the Fyfe Hills - Khmara Bay region, Enderby land

Seydoux-Guillaume AM, Paquette JL, Wiedenbeck M, et al (2002) Experimental resetting of the U-Th-Pb systems in monazite. Chem Geol 191:165–181. https://doi.org/10.1016/S0009-2541(02)00155-9

Seydoux-Guillaume AM, Goncalves P, Wirth R, Deutsch A (2003) Transmission electron microscope study of polyphase and discordant monazites: Site-specific specimen preparation using the focused ion beam technique. Geology 31:973–976. https://doi.org/10.1130/G19582.1

Seydoux-Guillaume AM, Wirth R, Deutsch A, Schärer U (2004) Microstructure of 24-1928 Ma concordant monazites; implications for geochronology and nuclear waste deposits. Geochim Cosmochim Acta 68:2517–2527. https://doi.org/10.1016/j.gca.2003.10.042

Seydoux-Guillaume AM, Bingen B, Paquette JL, Bosse V (2015) Nanoscale evidence for uranium mobility in zircon and the discordance of U-Pb chronometers. Earth Planet Sci Lett 409:43–48. https://doi.org/10.1016/j.epsl.2014.10.044

Seydoux-Guillaume AM, Deschanels X, Baumier C, et al (2018) Why natural monazite never becomes amorphous: experimental evidence for alpha selfhealing. Am Mineral 103:824–827. https://doi.org/10.2138/am-2018-6447

Seydoux-Guillaume AM, Fougerouse D, Laurent AT, et al (2019) Nanoscale resetting of the Th/Pb system in an isotopically-closed monazite grain: A combined atom probe and transmission electron microscopy study. Geosci Front. https://doi.org/10.1016/j.gsf.2018.09.004

Shannon RD (1976) Revised Effective Ionic Radii and Systematic Studies of Interatomie Distances in Halides and Chaleogenides. Acta Crystallogr Sect A 32:768–771. https://doi.org/10.1107/S0567739476001563

Sheraton JW, Offe LA, Tingey RJ, Ellis DJ (1980) Enderby Land, Antarctica-an unusual Precambrian high-grade metamorphic terrain. J Geol Soc Aust 27:1–18. https://doi.org/10.1080/00167618008729114

Thompson K, Lawrence D, Larson DJ, et al (2007) In situ site-specific specimen preparation for atom probe tomography. Ultramicroscopy 107:131–139. https://doi.org/10.1016/j.ultramic.2006.06.008

Turuani MJ, Laurent AT, Seydoux-Guillaume AM, et al (2022) Partial retention of radiogenic Pb in galena nanocrystals explains discordance in monazite from Napier Complex (Antarctica). Earth Planet Sci Lett 588:117567. https://doi.org/10.1016/j.epsl.2022.117567

Utsunomiya S, Palenik CS, Valley JW, et al (2004) Nanoscale occurrence of Pb in an Archean zircon. Geochim Cosmochim Acta 68:4679–4686. https://doi.org/10.1016/j.gca.2004.04.018

Valley JW, Cavosie AJ, Ushikubo T, et al (2014) Hadean age for a post-magma-ocean zircon confirmed by atom-probe tomography. Nat Geosci 7:219–223. https://doi.org/10.1038/ngeo2075

Valley JW, Reinhard DA, Ushikubo T, et al (2015) Nano- and micro-geochronology in Hadean and Archean zircons by atom-probe tomography and SIMS: New tools for old minerals. Am Mineral 100:1355–1377. https://doi.org/10.2138/am-2015-5134

Varga J, Raimondo T, Daczko NR, Adam J (2020) Experimental alteration of monazite in granitic melt: Variable U–Th–Pb and REE mobility during melt-mediated coupled dissolution-precipitation. Chem Geol 544:119602. https://doi.org/10.1016/j.chemgeo.2020.119602

Verberne R, Reddy SM, Saxey DW, et al (2020) The geochemical and geochronological implications of nanoscale trace-element clusters in rutile. Geology XX:1–5. https://doi.org/10.1130/g48017.1

White LF, Darling JR, Moser DE, et al (2017) Atomic-scale age resolution of planetary events. Nat Commun 8:1–6. https://doi.org/10.1038/ncomms15597

Whitehouse MJ, Kusiak MA, Wirth R, Ravindra Kumar GR (2017) Metallic Pb nanospheres in ultra-high temperature metamorphosed zircon from southern India. Mineral Petrol 111:467–474. https://doi.org/10.1007/s00710-017-0523-1

Wyckoff RWG (1963) Crystal Structures, 2nd edn. Interscience, New York

Figures, tables and captions

Fig. 1 a: Maps location of Casey Bay in the Napier Complex and the emplacement of Zircon Point in Casey Bay. b: Geological map of Zircon Point and location of the sampling site after Black et al (1983a). c: SEM-BSE imaging showing fractured garnet, sillimanite and rutilated quartz, the plagioclase corona surrounding garnet and sillimanite (white arrows) and the breakdown of garnet in secondary biotite. Monazite grain corresponds to MzA15. Bt2 = secondary biotite, Gt = garnet, Mnz = monazite, rt-Qz = rutilated quartz, Sil = sillimanite

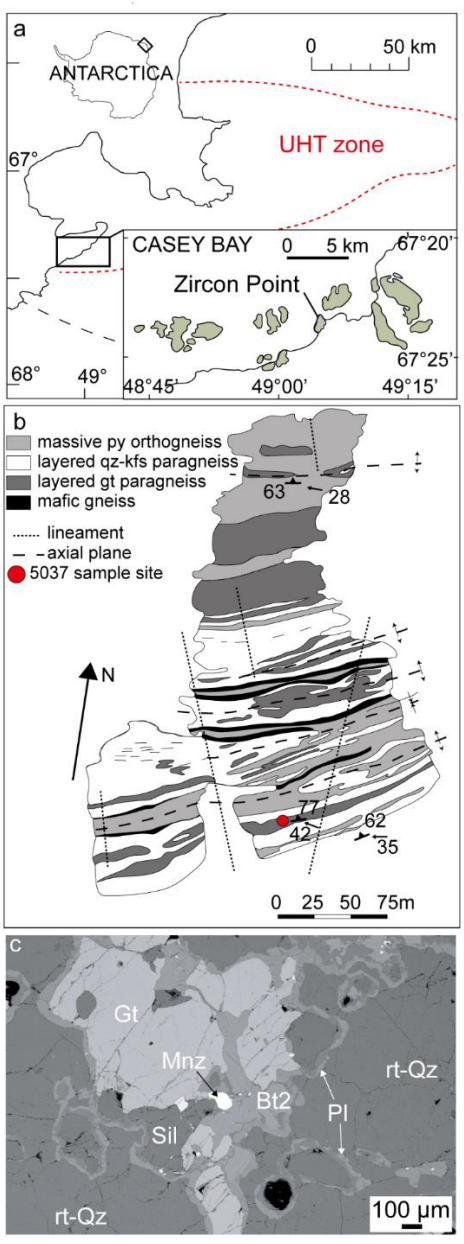

Fig. 2 BSE imaging of 9 monazite grains sharing variety of textural features. On the first line from the left to the right; growth zoning (Mnz17), oscillatory zoning (Mnz2), a small dark core surrounded by a large bright rim (MzA2) and a large dark core surrounded by several bright rims (Mnz16). The second line present grains showing bright lines crossing cores and in some cases rims (Mnz4). Grains on the third line show high amount of bright and dark dots corresponding to distinct nanophases within monazite crystal bigger in cores than rims. Comparison of BSE and SE images from the same area (Mnz25-FIB3 location) showing that dark nanophases correspond to low relief while bright nanophases show no relief. There is no surface difference between the core and the rim. Textural position indicates for each grain. Red rectangles indicate FIB-foil locations and red circles APT specimen locations. If not specified, scale bars: 10 µm

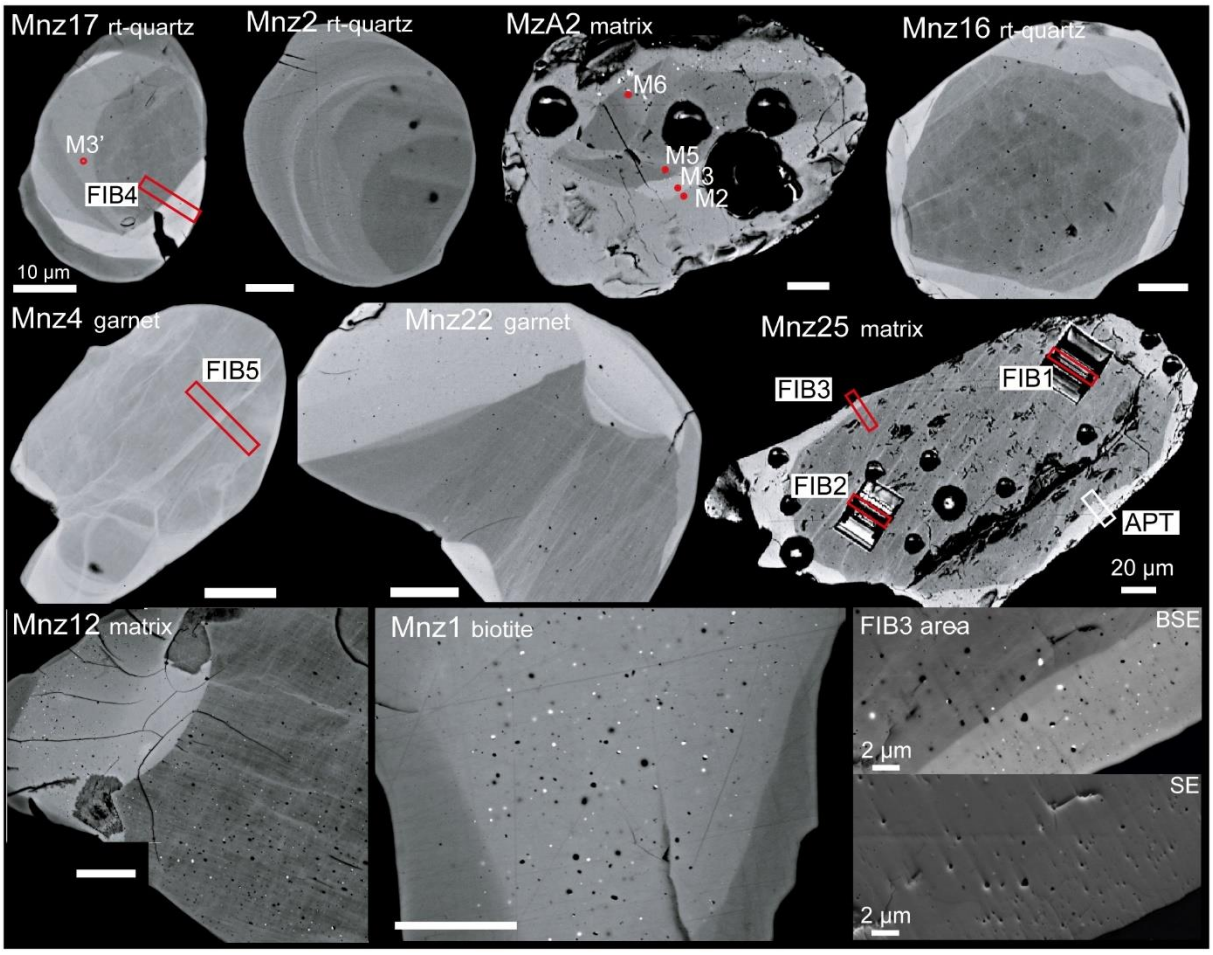

Fig. 3 Mnz13 characterization. a: BSE image showing bright core containing bright lines and bright and dark dots, surrounded by a dark rim presenting oscillatory zoning (white arrow). BSE (b) and SE (c) imaging of the core showing textural features in detail as bright and dark dots some of them reaching a size of 0.5 µm in diameter, bright lines (dark and white arrows in b) and fractures crossing the core. Bright and dark dots in BSE image show respectively no and low relief trend on SE image. The largest bright lines ~ 0.5 µm wide (black arrow) form a broad network while the thinnest (white arrow), less than 0.1 µm wide form a thin grid pattern which intersect with an angle of 60°. The network is not revealed on the grain surface. d: BSE imaging of the rim showing bright and dark dots with a size significantly smaller than those in the core, less than 0.1 µm in diameter. e: Qualitative map of Th highlighting high-Th core and low-Th rim texture and Th-rich lines in the core. f: Grain reduction orientation deviation (GROD) angle map obtained by EBSD. Observed disorientations are related to fractures crossing the grain

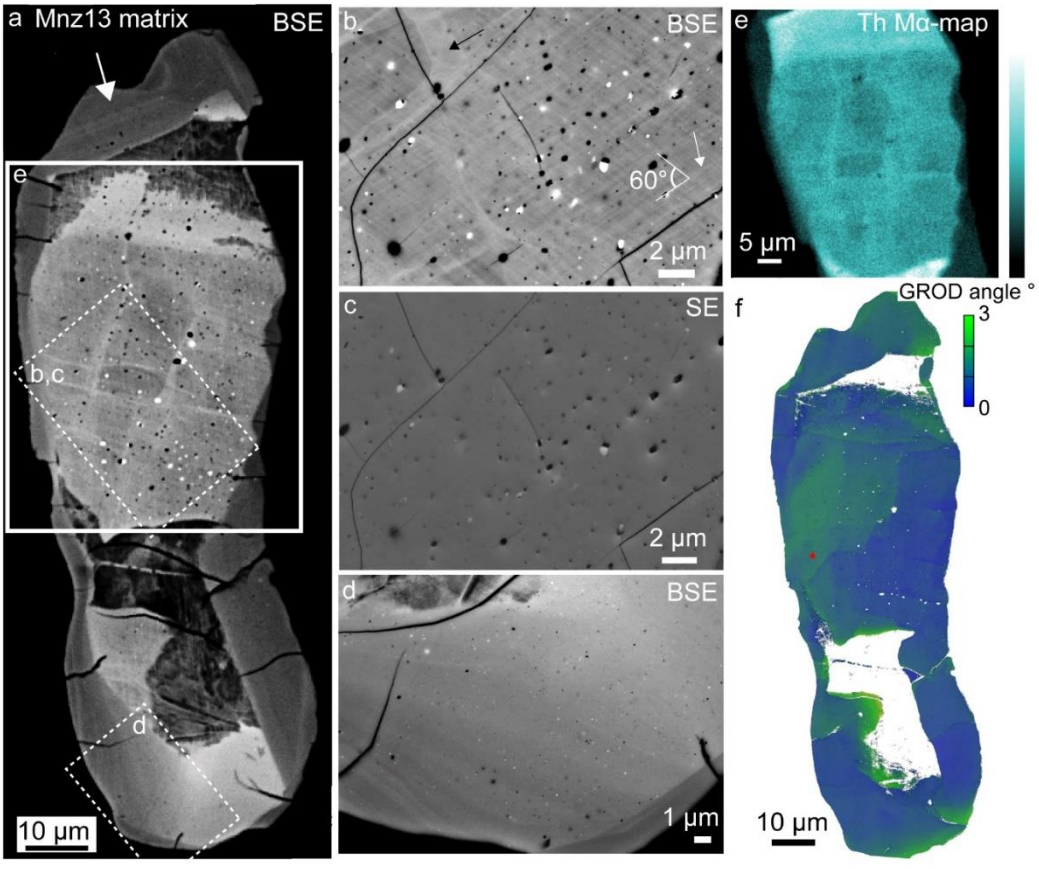

Fig. 4 Chemical composition of monazite. Ternary diagram constructed with the cheralite ($CaTh(PO_4)_2$), huttonite ($ThSiO_4$) and monazite ($REEPO_4$) end members. Chemical variations within grain is not related to the internal features such as rim or core with the term core also includes homogeneous grains

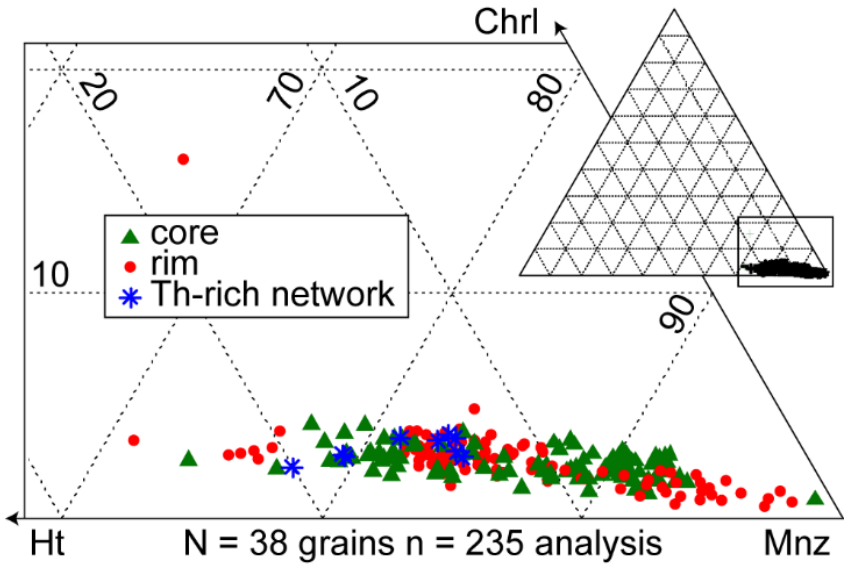

Fig. 5 TEM results. a: STEM-ADF image of Mnz25-FIB2 targeting a coarse Th-rich network ramification in the core of monazite Mnz25 located in the matrix. Th-rich network is marked by a brighter area reflecting chemical variation with high Th content in this area compare to the monazite core. Note the presence of nanophases isolated or polyphased (bright and dark contrasts). Dark contrasts are due to FIB artefacts (curtaining due to the nanophase). TEM-BF (b) and STEM-ADF (c) images of a nanophase within monazite (2). TEM-BF image shows Bragg diffraction contrasts (dark) in (1) indicate the crystalline state of this domain and bright contrast on STEM-ADF image indicated that it consists of high-density material. The part (3) shows no Bragg diffraction contrast (b) reflecting the amorphous state of the area that is composed of low-density material indicated by the darker contrasts on STEM-ADF image (c). EDS analyses on this nanophase are given figure 8a. d: STEM-ADF image of Mnz25-FIB3 targeting the rim of Mnz25 showing nanophases isolated or polyphased with sizes between 20 up to 200 nm in diameter. e: STEM-ADF image of Mnz4-FIB5 from monazite located in garnet mostly showing polyphased nanophases with sizes between 20 up to 250 nm. Note the higher number of nanophases in Mnz4-FIB5. The crystalline part (1) appears to be polycrystalline (f). FIB-foils location is given figure 2

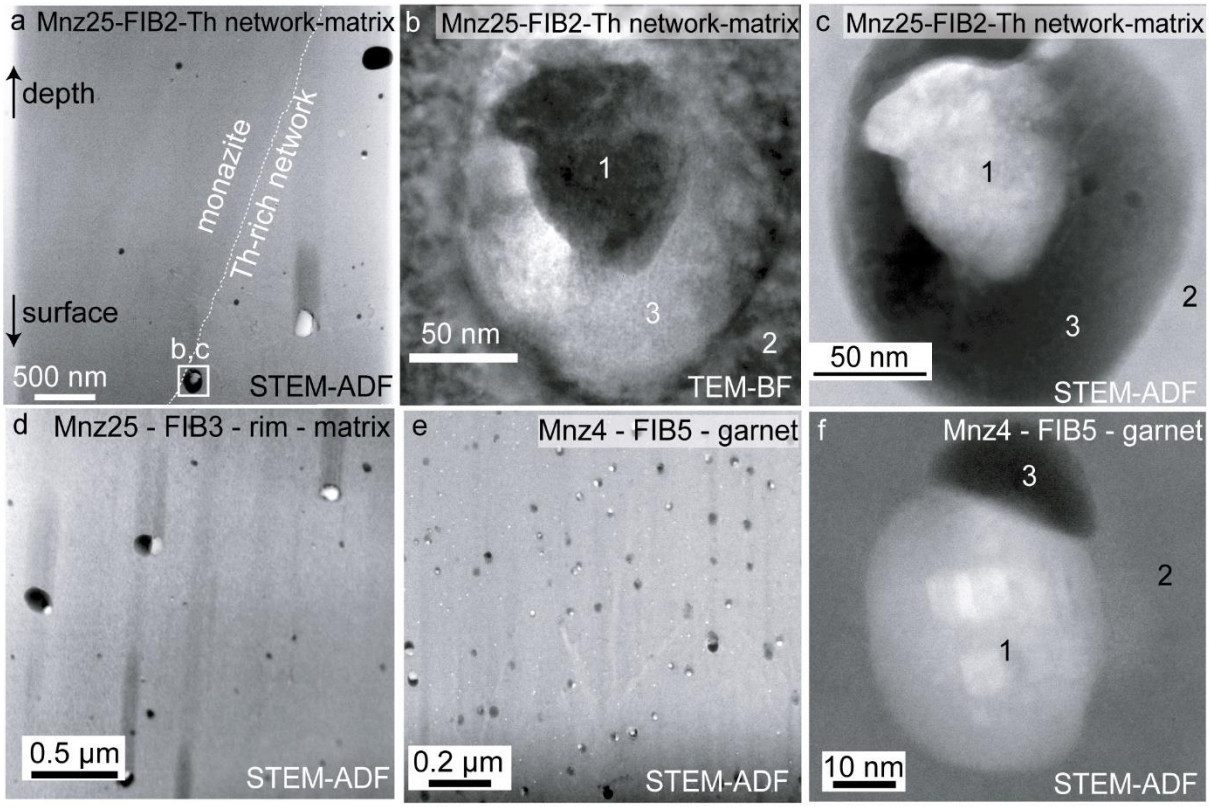
a Mnz25-FIB2-Th network-matrix
depth
surface
monazite
Th-rich network
b,c
500 nm
STEM-ADF
b Mnz25-FIB2-Th network-matrix
1
3
2
50 nm
TEM-BF
c Mnz25-FIB2-Th network-matrix
1
2
3
50 nm
STEM-ADF
d Mnz25 - FIB3 - rim - matrix
0.5 µm
STEM-ADF
e Mnz4 - FIB5 - garnet
0.2 µm
STEM-ADF
f Mnz4 - FIB5 - garnet
3
2
1
10 nm
STEM-ADF

Fig. 6 Diffraction pattern of nanophases. TEM-BF images showing galena in Mnz25-FIB1 from monazite in matrix (a) and phase 2 in Mnz4-FIB5 from monazite in garnet (c). Note the Bragg diffraction contrasts in nanophases and the typical mottled diffraction contrast of monazite. b, d: Diffraction patterns obtained on nanophases shown on a and c (selected area corresponds to the white circle), presenting diffraction spots of galena (b) and diffraction spots of both monazite and phase 2 (d). On d, only diffraction spots from phase 2 are measured. FIB-foils location is given figure 2

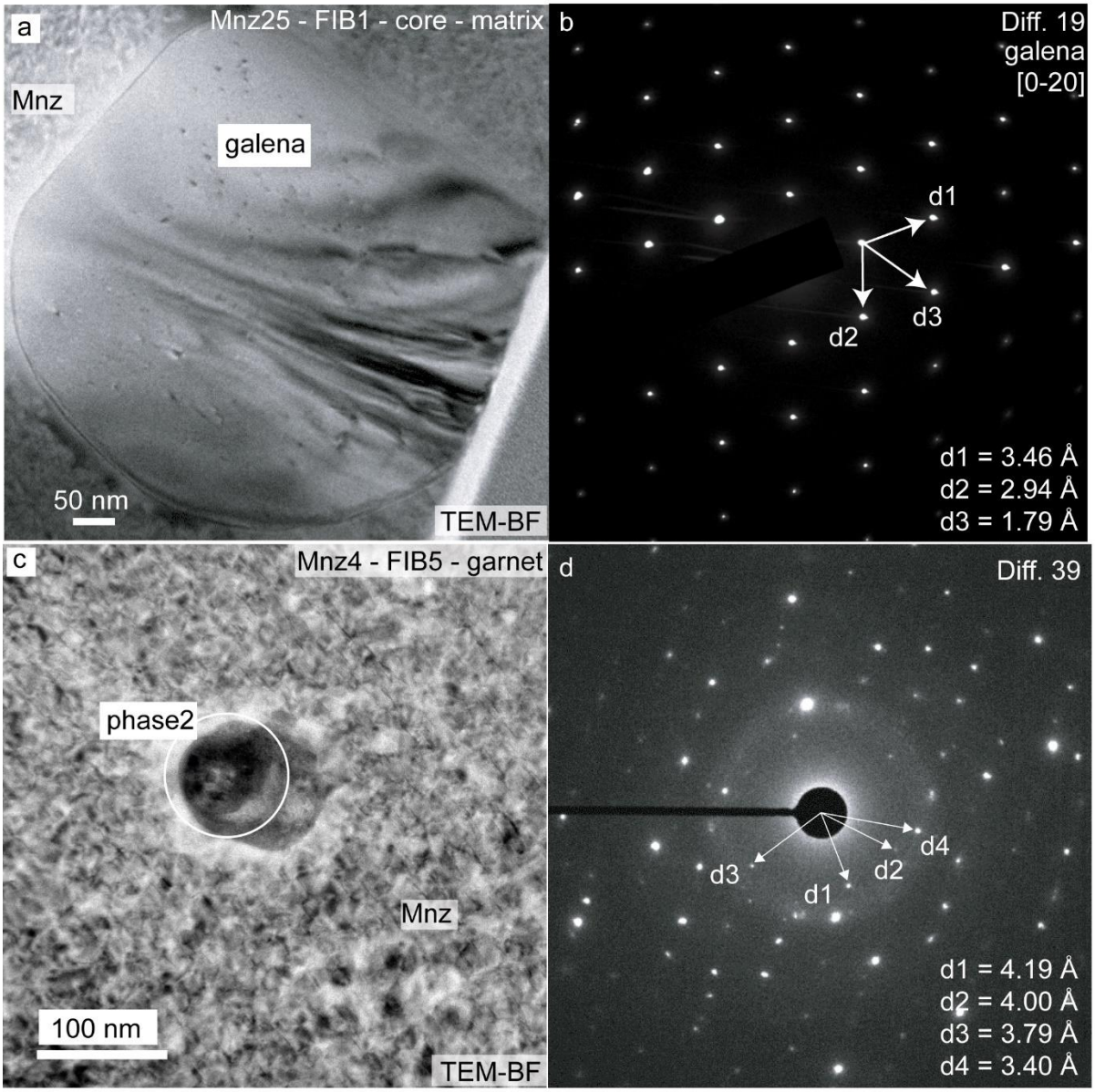

Table 1 d-spacings in Ångström of nanophases of this study compare to published values for native Pb, PbS and Pb-oxides

d(hkl) observed Mnz4-FIB5		Mnz25-FIB1	Pb cubic	PbS cubic	PbO orthorombic	tetragonal	PbO_2 orthorombic	tetragonal	Pb_2O_3 monoclinic	Pb_3O_4 tetragonal
Phase3	Phase2	Phase1	metal	Galena	Massicot	Litharge	Scrutiniyite	Plattnerite	Sesquioxyde	Minium
no PbS, no metal Pb	Pb_2O_3	PbS	a=b=c= 4.9505	a=b=c= 5.9362	a=5.8931 b=5.4904 c=4.7528	a=b=3.9744 c=5.0220	a=4.9470 b=5.9510 c=5.4970	a=b=4.9577 c=3.3879	a=7.814 b=5.627 c=8.465	a=b=8.8110 c=6.5630
	4.19 (n=3)			4.198					4.232	
	4.00 (n=3)				4.017	3.974	4.038		3.876	3.94
	3.79 (n=2)				3.7		3.804		3.785	3.658
		3.46 (n=2)	3.501	3.427	3.593			3.506	3.49	
	3.40 (n=3)							3.388	3.382	3.378
3.06					3.068	3.117	3.128		3.024	3.075
2.96		2.94	2.858	2.968	2.947	2.81	2.975	2.797	2.966	2.937
2.17 (n*=2)			2.214	2.099	2.181	2.123	2.228	2.217	2.19	2.188
		1.79		1.79	1.797	1.777	1.798	1.753	1.794	1.79
1.77			1.75		1.753		1.757		1.779	1.755
1.57			1.566	1.587	1.555	1.558	1.564	1.568	1.56	1.506
			Wyckoff 1963		Hill 1985	Boher et al 1985	Wyckoff 1963	Bolzan et al 1997	Bouvaist et Weigel 1970	Gavarri 1975

*n = number of d-spacing measured

Fig. 7 STEM-ADF images of clusters (a, b, c) in Mnz25-FIB3 showing bright contrasts reflecting the concentration of high-density material in cluster with a size of 2-5 nm. Clusters are surrounded by a dark contrast area slightly off-center (b, c). Bright dots correspond to the atomic columns of heavy atoms (REE, Th) of the monazite (e). d: FFT of the STEM-ADF image of the cluster in c showing diffraction spots from monazite in [001] zone axis. e: Crystallographic model representing Ce atoms. A Gaussian low-pass filter for noise reduction was applied to high-magnification STEM image c. FIB foil location is given figure 2

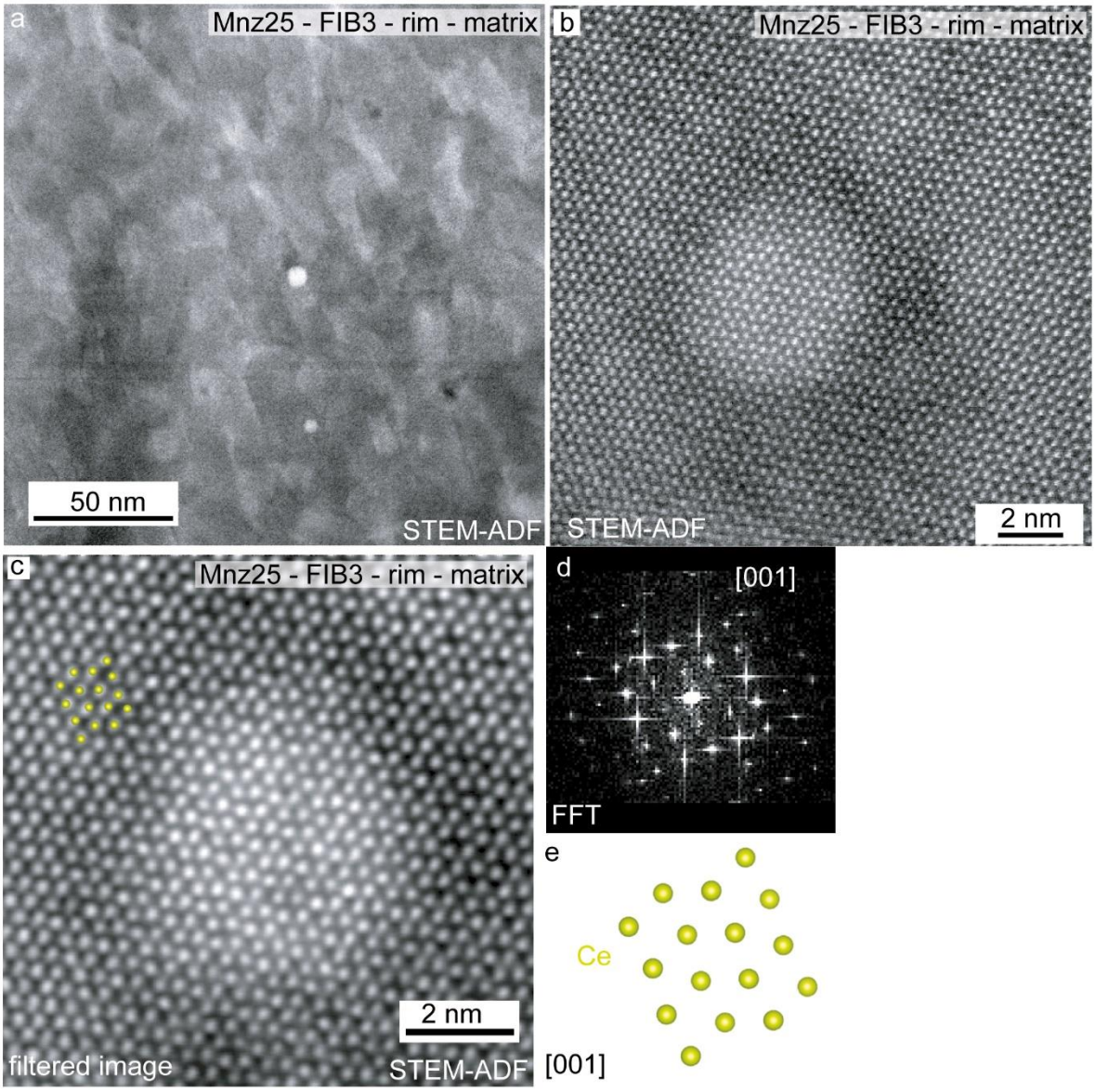

Fig. 8 Composition of Pb-bearing nanophases. a: EDS spectra obtained with TEM in Mnz25-FIB2 on three areas; bright crystalline zone on STEM-ADF (red spectrum) mainly composed of Pb, dark amorphous zone (black spectrum) containing Si, Mg, Al and Fe and monazite (grey spectrum). The nanophase is also shown figures 5b, c. b: EDS spectra obtained with TEM in Mnz17-FIB4 on three areas; dark crystalline zone of STEM-ABF (red spectrum) composed of Pb, bright zone (black spectrum) composed of Fe and S and monazite (grey spectrum). Note the presence of Cu peak due to the use of Cu-grid to hold FIB-foils. FIB-foils location is given figure 2

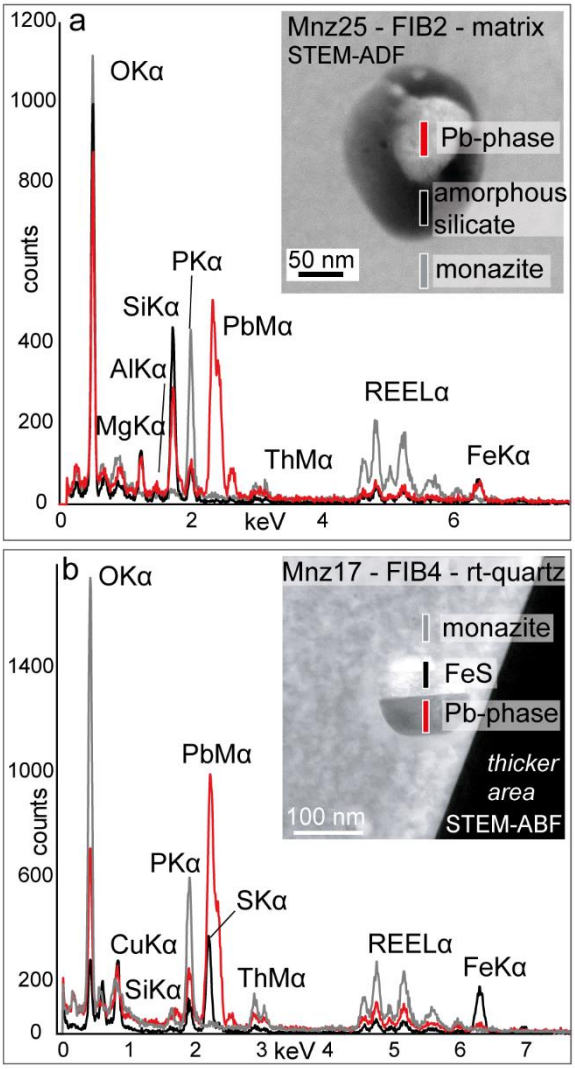

Fig. 9 EDS spectra obtained in monazite matrix (black) and cluster (red) showing in details O, Si and P peaks. Note the presence of high Pb content and slight increase in Si in the cluster with slight decrease in O and P compare to monazite

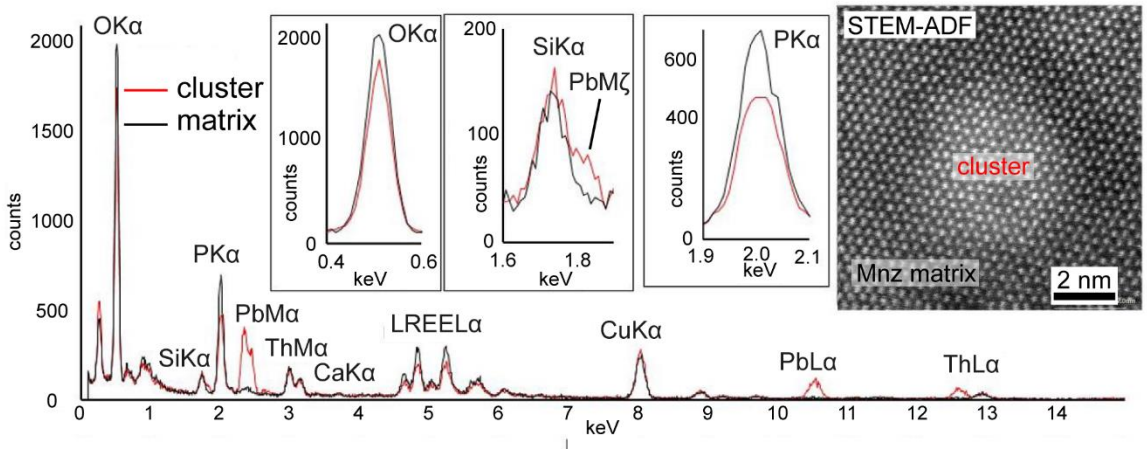

Fig. 10 a: APT reconstruction of M16 from Mnz25 specimen targeting a thin ramification of the Th-rich network. Thorium isoconcentration at 0.15 at. % highlight the feature. Si enriches in the Th-rich network. Distribution of Pb and Si show a heterogeneous distribution forming nanoscale features of 20 nm localized in the Th-rich network and Al is heterogeneously distributed, highlighting Al enrichments in some Pb-Si nanoscale features. b: APT reconstructions of specimen M19 from Mnz25 showing Pb, Si, Mg and Al heterogeneous distributions and concentration forming a nanoscale feature of 30 nm in diameter. Sulfur distribution is homogeneous. Pb distribution also shows clumps of 10 nm correlated with Ca and Si clumps corresponding to clusters identified with TEM. c: APT reconstruction of M6 from MzA2 targeting a galena and showing Pb, S Ce and Th distributions highlighting interface between monazite where Ce and Th are localized and galena where Pb and S are concentrated. One dot = one atom. Specimens location is given figures 2 and S7

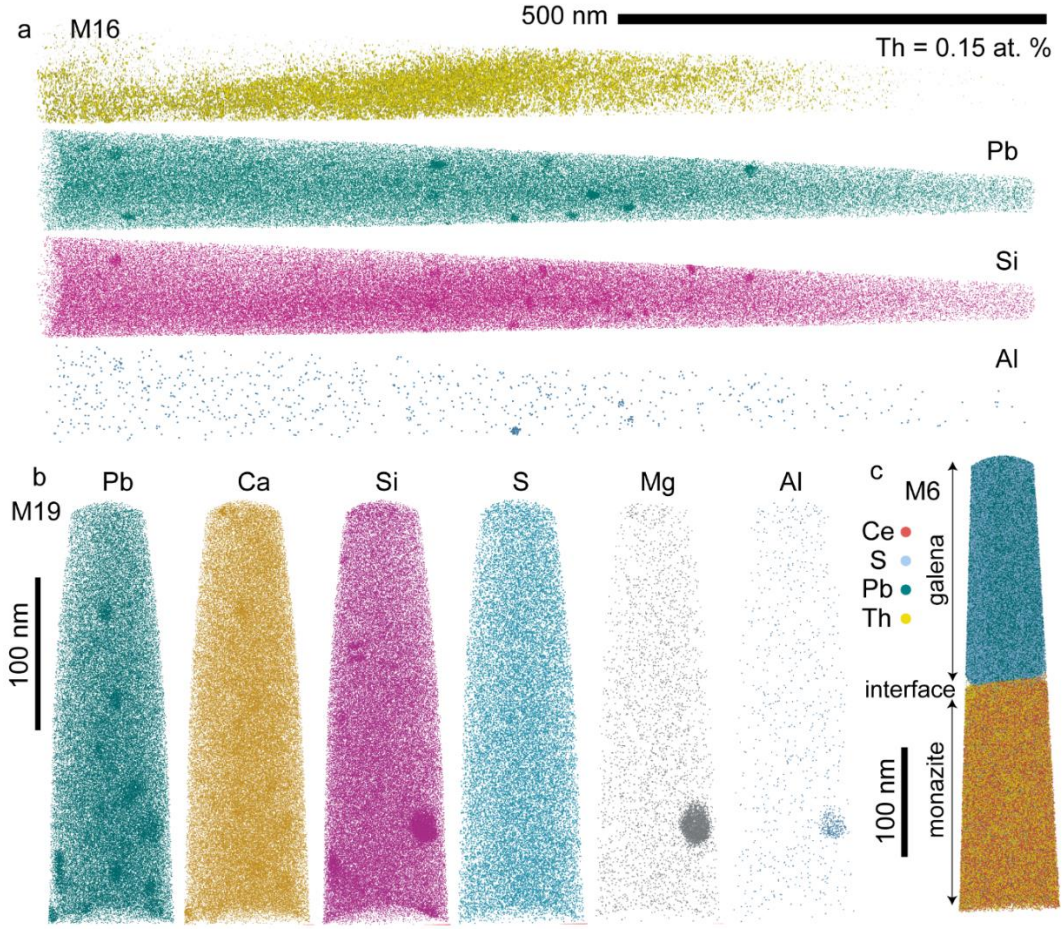

Fig. 11 a: APT reconstruction of M15 from Mnz25 specimen showing Pb and Si heterogeneous distribution forming clumps with a size < 10 nm and corresponding to clusters identified with TEM. b: Proxigram done with three interfaces defined by 0.7 at. % of Si showing a high increase in Pb and Si and a slight increase in Ca in clusters while Th remains constant between monazite and cluster. c: Pb vs. Si + Ca diagram done with 34 compositions taken from profiles, and showing a distribution broadly around the 1:1 line for the Pb-Ca-Si and Pb-Si groups while Pb-Ca group plot around the 1:2 line. Specimen location is given figure S7

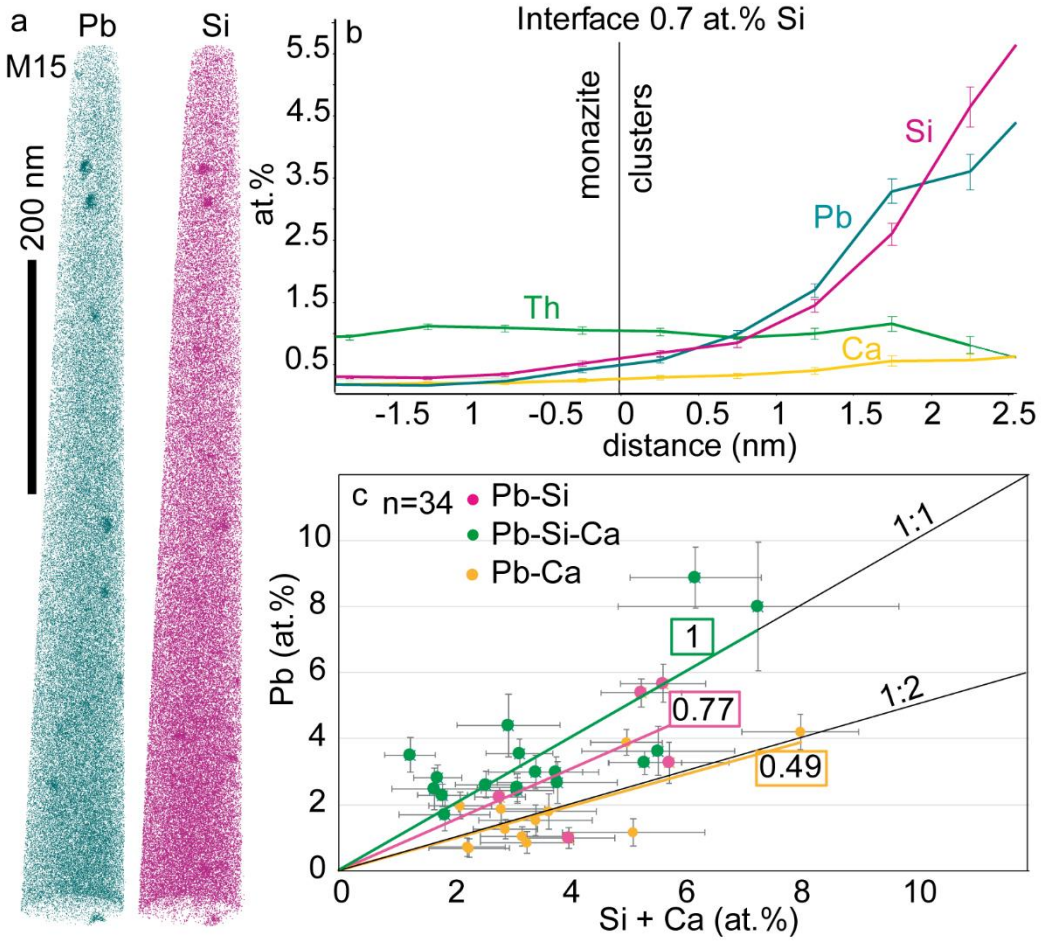

Table 2 Classification of the different features identified (Th-rich network, Pb-bearing nanophases and clusters) with the different properties in several techniques used from the micro- to the nanoscale

		Th-rich network	**Pb-bearing nanophases**		**Clusters**
Microscale features					
SEM, EPMA		diffuse, linear to wavy, forming a thin grid pattern or a coarse network dominated by high Th ±Si low REE, P and Y (Figs. 3, S1-S3)	bright and dark contrast on BSE images forming dots with various size but always < 1 µm, corresponding to nanophases isolated or polyphased (Figs. 2, 3) and highlighted by chemical variations in Pb, Si, S, Mg, Al, Fe (Figs. S1-S3)		-
Nanoscale features					
TEM	structure	diffuse, brighter contrasts on STEM-ADF image (Fig. 5a)	isolated or polyphased of 20-500 nm in size, consisting in: a crystalline part showing bright contrast on STEM-ADF image and dark contrast on TEM-BF image (Fig. 5), identified as PbS or Pb_2O_3 (Fig. 6)	an amorphous part showing dark contrast on STEM-ADF image and bright contrast on TEM-BF image (Fig. 5)	bright contrast on STEM-ADF image with a size < 10 nm surrounded by an area with dark contrasts; no difference in crystallographic lattice between monazite and cluster (Fig. 7)
	composition	increase of Th	crystalline part = Pb bearing (Fig. 8)	amorphous part = decoupled Ca and Si or Si ±Mg ±Al ±Fe or FeS (Fig. 8)	Pb ±Ca ±Si (Figs. 9, S6)
APT	composition	increase of Th and Si (Fig. 10)	Nanoscale features (> 20 nm) of Pb + Si + Mg + Al + Fe or Pb + Ca ±Si or Pb + S (Figs. 10, S8-S13)		clumps (< 10 nm) Pb ±Ca ±Si (Figs. 11, S8-S12)

Fig. 12 Schematic model for clusters and Pb-bearing nanophases formation related to geochronological history (complementary information are given Fig. S14). Stage I representing an oriented monazite lattice that crystallized at 2.44 Ga. Th and U decay in Pb induce charge deficit and radiation damage. Stage II: recoil nucleii induce high damage along ~10 nm favouring mobility of Pb and Ca + Si initially associated with Th and U forming clusters whose trapping is favoured by α-healing mechanism. Stages I and II occurring simultaneously from 2.44 Ga to 1.02 Ga and inducing cluster formation. Stages III and IV: fluid ingress inducing dissolution-precipitation and monazite replacement. Pb* is mobilized by fluid. Fluid saturation at the advancing reaction front induce Pb-bearing nanophases precipitation. Stages III and IV occurring simultaneously at 1.02 Ga. Stage I bis and II bis: Th and U decay, mobility of Pb and Ca + Si and trapping favoured by α-healing mechanism, occurring simultaneously inducing cluster formation and representing the actual state of monazite grains hosted in garnet and rt-quartz. Stages III bis to IV bis and I ter to II ter occurred only in monazite grains hosted in the quartzo-felspathic matrix. Stages III bis and IV bis: fluid ingress inducing dissolution-precipitation, Pb, Ca and Si mobilisation, the resetting of very local nanodomains in monazite (due to low grade metamorphic conditions; Fig. S14) and the precipitation of Pb-bearing nanophases at 0.55 Ga. Stage I and II ter: Th and U decay, mobility of Pb and Ca + Si and trapping favoured by α-healing mechanism, occurring simultaneously in monazite inducing the present state of monazite grains hosted in matrix

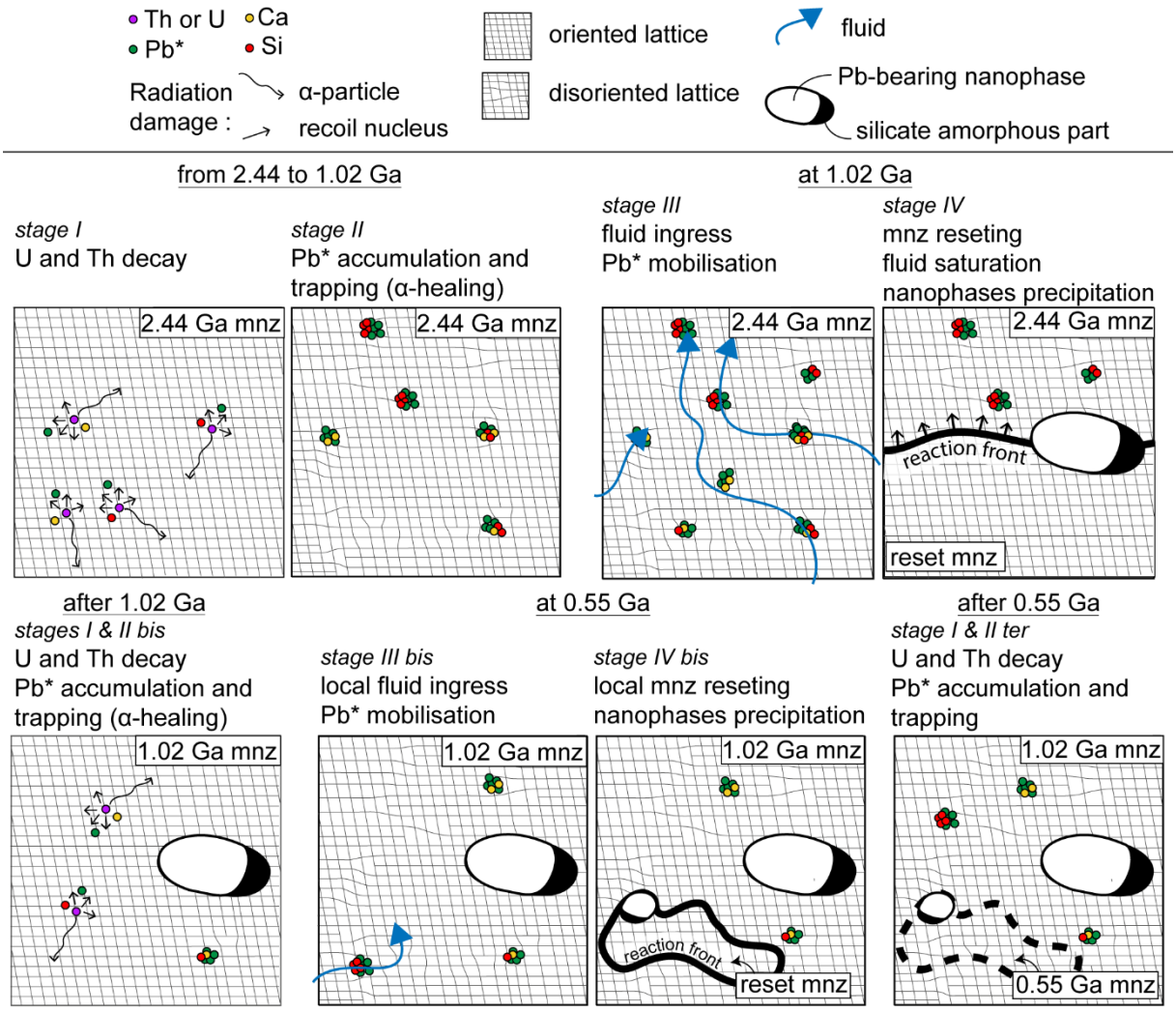
Th or U
Ca
Pb*
Si
Radiation damage :
α-particle
recoil nucleus
oriented lattice
disoriented lattice
fluid
Pb-bearing nanophase
silicate amorphous part
from 2.44 to 1.02 Ga
at 1.02 Ga
stage I
U and Th decay
stage II
Pb* accumulation and trapping (α-healing)
stage III
fluid ingress
Pb* mobilisation
stage IV
mnz reseting
fluid saturation
nanophases precipitation
2.44 Ga mnz
reaction front
reset mnz
after 1.02 Ga
at 0.55 Ga
after 0.55 Ga
stages I & II bis
U and Th decay
Pb* accumulation and trapping (α-healing)
stage III bis
local fluid ingress
Pb* mobilisation
stage IV bis
local mnz reseting
nanophases precipitation
stage I & II ter
U and Th decay
Pb* accumulation and trapping
1.02 Ga mnz
0.55 Ga mnz